Seasonal land ice-flow variability in the Antarctic Peninsula

Karla Boxall[1], Frazer D. W. Christie[1], Ian C. Willis[1], Jan Wuite[2] and Thomas Nagler[2]

[1]Scott Polar Research Institute, University of Cambridge, Cambridge, United Kingdom
[2]ENVEO IT GmbH, Innsbruck, Austria

5   *Correspondence to*: Karla Boxall (kb621@cam.ac.uk)

Abstract

Recent satellite-remote sensing studies have documented the multi-decadal acceleration of the Antarctic Ice Sheet in response to rapid rates of concurrent ice-sheet retreat and thinning. Unlike the Greenland Ice Sheet, where historical, high temporal resolution satellite and in situ observations have revealed distinct changes in land ice flow across intra-annual timescales, similar seasonal signals have not previously been observed in Antarctica. Here, we use high spatial and temporal resolution Copernicus Sentinel-1A/B synthetic aperture radar observations acquired between 2014 and 2020 to provide the first evidence for seasonal flow variability of the land ice feeding George VI Ice Shelf (GVIIS), Antarctic Peninsula. Our observations reveal a distinct austral summertime (December – February) speedup of ~0.06 ± 0.005 m d^{-1} (~22 ± 1.8 m yr^{-1}) at, and immediately inland of, the grounding line of the glaciers nourishing the ice shelf, which constitutes a mean acceleration of ~15% relative to baseline (timeseries-averaged) rates of flow. These findings are corroborated by independent, optically derived velocity observations. Regional contrasts in the onset of ice-flow acceleration and the overall timing of the speedup events across GVIIS fingerprint oceanic forcing as the primary control of this seasonality. Our findings imply that analogous ice-ocean interactions may be ongoing at the grounding lines of other ocean-vulnerable outlet glaciers around Antarctica. Assessing the degree of seasonal ice-flow variability at such locations is important for quantifying Antarctica's future contribution to global sea-level rise.

1.   Introduction

Three decades of routine Earth observation have revealed the progressive demise of the Antarctic Ice Sheet, evinced by accelerated rates of ice thinning, retreat and flow (Gardner et al., 2018; Konrad et al., 2018; The IMBIE Team, 2018; Rignot et al., 2019). This phenomenon has been ascribed to an array of atmospheric and oceanic forcing mechanisms impinging upon the continent (Thoma et al., 2008; Joughin et al., 2012a; Steig et al., 2012; Dutrieux et al., 2014; Paolo et al., 2018), from which resulting land ice losses are estimated to have totalled an average of ~109 ± 59 gigatons per year since 1992 (The IMBIE Team, 2018). Alongside satellite altimetry and gravimetry based assessments of ice-mass change, this trend has partly been constrained from satellite-derived velocity measurements acquired sporadically throughout the year (Rignot et al., 2011a; Mouginot et al., 2012), under the implicit (and unverified) assumption that no discernible intra-annual (i.e., seasonal or shorter)

30 variability in ice-flow exists (cf. Greene et al., 2018). In terms of intra-annual ice-flow variability, a historic dearth of systematic, high temporal resolution observations has also limited the ability to search for such changes across Antarctica; this is in contrast to mid-latitude and Arctic ice masses, where the timing and magnitude of seasonal ice-flow variability is now well observed (Iken et al, 1983; Hooke et al, 1989; Zwally et al., 2002; Hoffman and Price, 2014; Moon et al., 2014; King et al., 2018). Within the context of recent ice-sheet modelling exercises (Seroussi et al., 2020; Edwards et al., 2021), knowledge

35 of any intra-annual variations in ice flow is critical for elucidating the processes controlling Antarctica's evolution in a changing climate.

In this study, we examine for and find evidence of seasonal ice-flow variability across the glaciers feeding the climatically vulnerable George VI Ice Shelf, Antarctic Peninsula. We use 6/12-day repeat-pass Copernicus Sentinel-1A/B synthetic

40 aperture radar imagery for this purpose, together with independent, 16-day repeat-pass observations acquired by the Landsat 8 Operational Land Imager. We then discuss the potential mechanisms responsible for driving the observed seasonal ice-flow signals upstream of George VI Ice Shelf, which we ascribe to intra-annual variability in ocean forcing.

2. George VI Ice Shelf

In this study, we investigate seasonal ice-flow variability across 21 glaciers feeding the glaciologically compressive George

45 VI Ice Shelf (GVIIS) (Fig. 1). After Larsen C Ice Shelf, GVIIS is the second largest of the remaining ice shelves fringing the Antarctic Peninsula (Holt et al., 2013), and has an areal extent of 23,500 km^2. Ice-shelf flow bifurcates and advects towards both its northern (Marguerite Bay) and southern (Ronne Entrance) ice fronts at an average rate of 0.7 m d^{-1} (255 m yr^{-1}), with flow averaging 0.08 m d^{-1} (30 m yr^{-1}) and 1.1 m d^{-1} (400 m yr^{-1}) along its Alexander Island and Palmer Land margins, respectively (Fig. 1). The thickness of the ice shelf ranges between approximately 100 and 600 m (Morlighem et al., 2020).

50
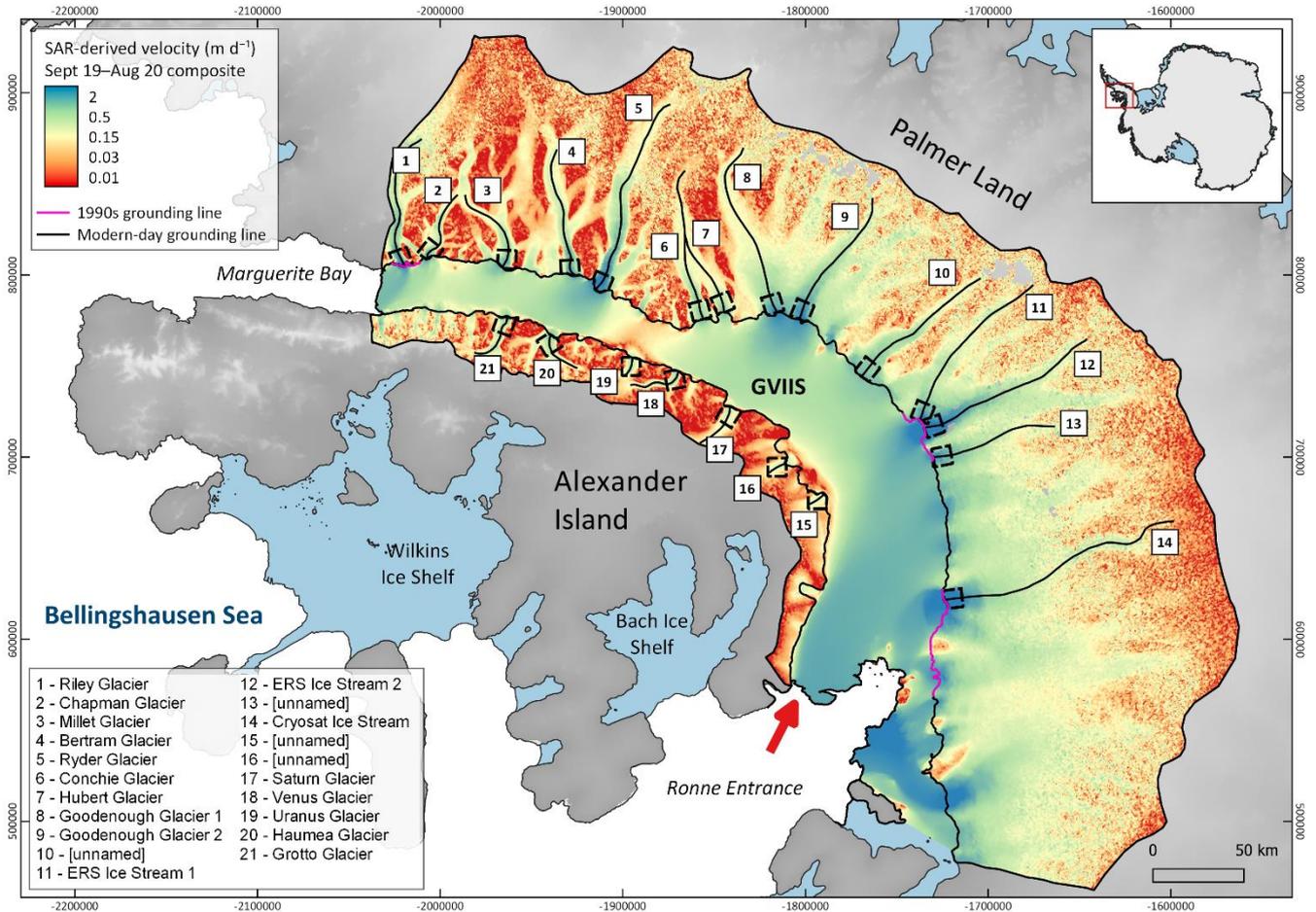
Figure 1 - Ice flow of George VI Ice Shelf (GVIIS) and its drainage basins derived from Sentinel-1A/B synthetic aperture radar-derived observations acquired between 2019 and 2020. Where data coverage exists, the landward margins of GVIIS are delineated using the modern-day (2018-2020) grounding line (black) and, elsewhere, its position as imaged in the 1990s (pink; cf. Sect. 3.1). Drainage basin limits are from Mouginot et al. (2017). Background DEM is the Reference Elevation Model of Antarctica (Howat et al., 2019). Numbered flowlines represent outlet glaciers draining to GVIIS (named according to the UK Antarctic Place-names Committee), and the 10 km² dashed boxes located inland of the grounding line of these glaciers indicate the averaging regions used in the production of Figs. 4, A1, A2 and D1. Map projection: EPSG:3031. Inset map shows location. Arrow indicates the region of dominant CDW inflow as inferred from in situ ocean observations (Jenkins and Jacobs, 2008; see Sect. 5.2 for further discussion).

Elsewhere in the Antarctic Peninsula, historical satellite observations have documented the abrupt, climate-driven disintegration of several ice shelves and the consequent dynamic acceleration of upstream glacial ice (Rott et al., 1996; Rack and Rott, 2004; Rignot et al., 2004; Scambos et al., 2004); this acceleration has increased Antarctica's net contribution to global sea-level (Scambos et al., 2004; The IMBIE Team, 2018). These events have been attributed primarily to the surface warming-induced presence of supraglacial meltwater lakes (Dirscherl et al., 2021), which are surmised to have instigated a process of rapid ice-shelf hydrofracture and collapse (Scambos et al., 2000; Banwell et al., 2013; Leeson et al., 2020). These phenomena have, in turn, been linked to an Antarctic Peninsula-wide amplification in surface temperatures over most of the

observational record (Vaughan et al., 2003). At GVIIS, supraglacial meltwater presence has been observed over the ice shelf since routine satellite observations began (Kingslake et al., 2017; Bell et al., 2018; Banwell et al., 2021), leading to the
70 identification of GVIIS as a potential site for future ice-shelf disintegration (Holt et al., 2013). Recent modelling studies suggest that resultant land ice losses associated with such an event would contribute an ~8 mm rise in global sea-level by 2100 (Schannwell et al., 2018).

In addition to the effects of supraglacial meltwater, ocean-driven basal melting has had, and will likely continue to have, an
75 important role in the evolution of GVIIS and its upstream glaciers (Pritchard et al., 2009; Holt et al., 2013; Paolo et al., 2015; Naughten et al., 2018). This is due to the flooding of relatively warm (~1-2 °C), high-salinity (~34.7 PSU) circumpolar deep water (CDW) beneath and offshore from GVIIS' sub-ice shelf cavity (Jenkins et al., 2010; Jenkins and Jacobs, 2008). Aping the high rates of ice-shelf melting observed across the Amundsen and western Bellingshausen sectors in the past (Pritchard et al., 2012; Rignot et al., 2013; Christie et al., 2018), this CDW presence has driven basal melting of up to 7 m yr^{-1} at GVIIS
80 over the satellite era (Paolo et al., 2015; Adusumilli et al., 2018), and has been implicated as the primary mechanism responsible for the multi-decadal acceleration of GVIIS' fastest-flowing feeder glaciers (Hogg et al., 2017; Gardner et al., 2018; Winter et al., 2020).

3. Data and Methods

We use high spatial-temporal resolution, all-weather, day/night imaging Copernicus Sentinel-1A/B synthetic aperture radar
85 (SAR) observations as our primary data source to both survey the seaward extent of the outlet glaciers feeding GVIIS and examine for seasonal variability in their flow. The methods used for these purposes are detailed below.

3.1 Grounding line delineation

Grounding lines are sensitive indictors of climate change and represent the boundary between seaward-flowing, terrestrial ice and adjoining, floating ice shelves. In parts of West Antarctica — including the Amundsen and western Bellingshausen sectors,
90 especially — grounding lines have retreated pervasively in response to ocean forcing over the past ~40 years (Park et al., 2013; Rignot et al., 2014; Christie et al., 2016; 2018; Konrad et al., 2018). In comparison to the detailed knowledge of grounding-line migration within these sectors, there have been no comprehensive, spatially complete grounding line surveys at GVIIS since the mid-1990s (Rignot et al., 2016). Accurate and updated knowledge of GVIIS' grounding line is therefore required to distinguish precisely between grounded and floating ice, the latter of which can undergo significant velocity variations over
95 diurnal (tidal) to seasonal timescales or longer (Joughin et al., 2016; Rott et al., 2020).

To recover the location of GVIIS' modern-day grounding line, we employed double-differential interferometric SAR (DInSAR) processing techniques to all consecutive 6-day repeat-pass Sentinel-1A/B Interferometric Wide (IW) single look

complex (SLC) data acquired during extended austral wintertime (May-October) 2020. Extended austral wintertime imagery
100 was used to maximise phase coherence between successive image pairs which may be degraded due to the attenuation of radar
waves by summertime supraglacial water presence (cf. Sect. 2). Similar to earlier work (Park et al., 2013; Rignot et al., 2014;
Christie et al., 2016), we removed the topographical component of phase from each interferogram, in this case using the
Reference Elevation Model of Antarctica (REMA; Howat et al., 2019). Assuming ice creep to be common between each SAR
image, we then differenced all successive interferograms to locate the limit of tidally induced vertical ice-shelf flexure. This
105 limit is represented as the landward extent of a band of closely spaced fringes on double-differenced interferograms (Rignot
et al., 2011b), and is an accurate proxy for the true grounding line which cannot be recovered directly by satellite-based imaging
techniques (Fricker et al., 2009; Friedl et al., 2020).

To supplement our grounding line observations across regions of poor phase coherence during extended wintertime 2020, we
110 filled data gaps using recently generated (albeit spatially discontinuous) Sentinel-1-derived grounding line information from
2018 (Mohajerani et al., 2021). Where this was not possible, for example in areas of phase aliasing resulting from very fast ice
flow exceeding ⪆ 1.6 m d^{-1}, we used the 1994-1996 MEaSUREs grounding line dataset (Rignot et al., 2016; pink grounding
lines in Fig. 1).

3.2 Derivation of ice velocity

115 Land ice velocities upstream of GVIIS were retrieved from all successive Sentinel-1 IW SLC image pairs acquired between
October 2014 and August 2020 using a combination of coherent and incoherent offset tracking techniques as described in
Nagler et al. (2015, 2021) and Wuite et al. (2015). These 12-day repeat-pass image pairs, which reduced to 6-day repeat
following the launch of Sentinel-1B in April 2016, were then used to produce monthly composites of mean ice flow and
associated grids of uncertainty (1σ) and valid pixel count. If during composite creation an image pair crossed into the
120 neighbouring month between the reference and secondary images used to retrieve ice velocity, then it was weighted
accordingly (cf. Nagler et al., 2015; Wuite et al., 2015). Final grids of monthly ice velocity, uncertainty and pixel count were
outputted with a posting of 200 m and, like our double-difference interferograms, were geocoded from radar coordinates to
EPSG:3031 (Antarctic Polar Stereographic) projection. Using our updated GVIIS grounding line product (cf. Sect. 3.1 and
Fig. 1), floating ice was subsequently masked from all monthly velocity grids. Proximal to the grounding line, where
125 uncertainties associated with offset tracking techniques are typically much smaller relative to inland areas characterised by
steep terrain and/or slow-flowing ice (Mouginot et al., 2012), the mean standard error associated with our grids totals 0.005 m
d^{-1} (1.8 m yr^{-1}). This value is comparable to that of other SAR-derived velocity products (Rignot et al., 2017), and was
calculated according to:

130 $$SE = \frac{\sigma}{\sqrt{n}} \qquad\qquad\qquad (1)$$

Where SE denotes standard error, and σ and n denote the standard deviation and valid pixel count, respectively.

We averaged velocities over monthly timescales to minimise contamination associated with ionospheric and tropospheric delay between successive (6/12-day repeat pass) Sentinel-1 image acquisitions (Rosen et al., 2000; Selley et al., 2021). Moreover, across the Antarctic Peninsula, Sentinel-1A/B acquisitions are currently acquired in descending mode only (ESA, 2022), meaning that the velocity data utilised in this study represent the relative displacement of point targets in the satellite line-of-sight (LOS) direction only. Recent work has shown that below sub-monthly resolution, relative velocities can be subject to bias owing to radar penetration differences associated with the freezing state of the snow-firn-ice interface between image acquisitions (Rott et al., 2020). This phenomenon can induce shifts in the radar LOS distance to target by several meters (Joughin et al., 2018; Rott et al., 2020), resulting in either an under- or overestimation of velocities depending on the flow direction of the ice relative to LOS (Rott et al., 2020).

3.3 Detection of seasonal ice-flow variability

We examined for seasonal variations in ice flow using the methodology summarised in Fig. 2. First, we examined for spatial patterns of seasonal flow variability in our SAR-derived velocity datasets. We then supplemented our findings with intra-annual timeseries analyses at and proximal to the grounding line and corroborated observed patterns of ice-flow variation using independent satellite-derived observations. The methods associated with these analyses are discussed in Sects. 3.3.1, 3.3.2 and 3.3.3, respectively.
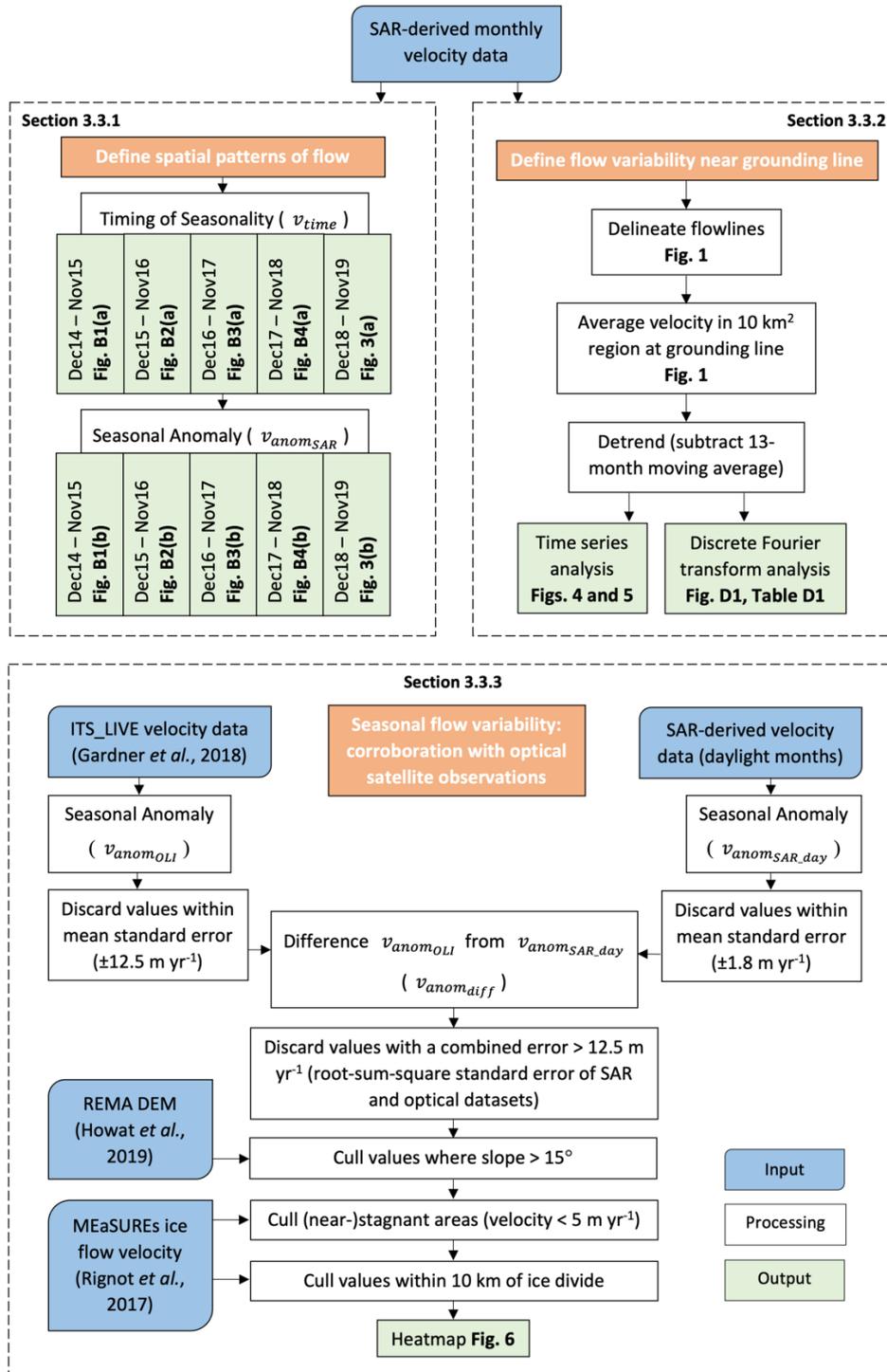
Figure 2 - Workflow detailing the establishment of spatial patterns of flow (Sect. 3.3.1), the assessment of flow variability near the grounding line (Sect. 3.3.2) and the corroboration with optical satellite observations (Sect. 3.3.3).

3.3.1 Spatial patterns of flow

Following Fig. 2, for each year spanning 2014 – 2019, we first constrained the month in which observed velocities were greatest on a pixelwise basis, v_{time}. This step was carried out to determine a) if a spatially coherent signal of ice-flow change was present upstream of GVIIS and, b) the season in which such a phenomenon occurred. Next, for each year (considered here to span December – November i.e., four complete seasons), the relative magnitude of any observed flow change was quantified in the form of a 'seasonal anomaly', $v_{anom_{SAR}}$. This metric is defined as the difference in median velocity for the season (either DJF, MAM, JJA or SON) in which v_{time} occurred, and the median across all other seasons that year. In the case of an austral summertime speedup associated with a maximum velocity observation in either December, January or February, for example, $v_{anom_{SAR}}$ is given by:

$$v_{anom_{SAR}} = (v_{12}, \widetilde{v_1}, v_2) - (v_3, \widetilde{..., v_{11}}) \qquad (2)$$

Where v_n denotes the velocity magnitude as observed during month n (v_1, January; ...; v_{12}, December) Using this notation, positive $v_{anom_{SAR}}$ indicates a greater median velocity during austral summertime compared with all other seasons. In our calculation of v_{time} and $v_{anom_{SAR}}$ above, pixels without continuous data coverage throughout the entire year were culled from our analyses. Pixels falling within standard error bounds (cf. Sect. 3.2) were also discarded.

3.3.2 Flow variability near the grounding line

To supplement our spatially resolved observations discussed above, we examined in more detail the temporal variations in ice-flow near the coast of the outlet glaciers shown in Fig. 1. To do this, we calculated mean monthly velocity and standard error within a 10 km² region located directly upstream of the grounding line between 2014 and 2020. Glaciers without sufficient modern-day grounding line coverage were excluded from further analysis (Fig. 1; cf. Sect. 3.1). Next, we removed long-term trends in velocity over each 10 km² region (cf. Hogg et al., 2017; Gardner et al., 2018) using a 13-month moving average (Fig. A1) to accentuate intra-annual trends. Finally, we quantified the dominant frequency of these trends using discrete Fourier transform analysis. In signal processing, this technique decomposes a time domain function into the frequency domain, from which its most dominant frequency (i.e., number of cycles per unit of time) and phase and amplitude characteristics can be identified (Bracewell, 1978). To enable direct quantitative comparison between outlet glaciers, we fitted a cosine wave optimised to the most dominant frequency observed across all outlet glacier timeseries and extracted their associated phase and amplitude, which in this case denotes the approximate timing and magnitude of the seasonal velocity signals, respectively.

3.3.3 Seasonal flow variability: corroboration with optically derived satellite observations

To supplement our SAR-based observations, we also calculated a similar seasonal metric, $v_{anom_{OLI}}$, to that described in Sect. 3.3.1 using independent, spatially-temporally collocated velocity information derived from Landsat 8 Operational Land Imager

(OLI) imagery acquired between 2014 and 2019 (Fig. 2). While Landsat 8's sun-synchronous orbit precludes any imaging outside extended austral summertime (September-April), derived velocity observations during this time offer an important dataset with which to corroborate any summertime ice-flow variability observed in the SAR record. This is due to the passive, on-nadir imaging characteristics associated with OLI which, unlike the SAR-based calculation of $v_{anom_{SAR}}$, are insensitive to any viewing geometry or snow/firn penetration-related biases (cf. Sect. 3.2). Any agreement between calculated values of $v_{anom_{SAR}}$ and $v_{anom_{OLI}}$ would therefore underscore the utility of our SAR-based methodology to detect extended summertime signals with confidence. Such agreement would, by extension, also imply a high degree of certainty in our ability to quantify ice-flow variability during non-daylight seasons.

We calculated $v_{anom_{OLI}}$ using Landsat 8-derived velocity grids acquired from the Inter-mission Time Series of Land Ice Velocity and Elevation (ITS_LIVE) data archive (Gardner et al., 2019). These grids were obtained for each unique Landsat granule over GVIIS and its environs, and represent velocities as constrained from featuring tracking of all successive 16-day repeat-pass Landsat 8 image pairs acquired between January 2014 to April 2019 (Gardner et al., 2018, 2019). In total, 817 image pairs were utilised in this study which, comparable to our Sentinel-1-derived velocity grids, have a mean standard error of <0.034 m d^{-1} (12.5 m yr^{-1}) (Gardner et al., 2018, 2019).

For a speedup during the austral summertime (DJF), for example, $v_{anom_{OLI}}$ was calculated using:

$$v_{anom_{OLI}} = \left(\widetilde{v2014_{12,1,2}, \ldots, v2019_{12,1,2}} \right) - \left(\widetilde{v2014_{3,4,9,10,11}, \ldots, v2019_{3,4,9,10,11}} \right) \tag{3}$$

Where $v2014_{12,1,2}$ denotes the median velocity magnitude as observed during December, January and February 2014, respectively; $v2019_{12,1,2}$, same but for 2019 (i.e., the end of the observational record) and $v2019_{3,4,9,10,11}$, velocity magnitude spanning all non-summertime daylight months for 2019. Similar to Eq. (2), positive $v_{anom_{OLI}}$ would indicate a greater median velocity observed during austral summertime than all other (non--summertime) daylight months. Unlike in our derivation of $v_{anom_{SAR}}$, we calculated the median of all summer months over the entire 2014-2019 period to maximise spatial coverage at the expense of temporal resolution. This was due to the preponderance of clouds in the Landsat record and resulting lack of velocity coverage at monthly resolution. Prior to any further analysis, values of $v_{anom_{OLI}}$ falling within standard error (<0.034 m d^{-1}) were removed.

To corroborate our SAR-derived metric (Sect. 3.3.1), we differenced $v_{anom_{OLI}}$ from a second measure of $v_{anom_{SAR}}$ whose temporal limits were clipped to match the daylight months imaged by Landsat 8 (September – April; Fig. 2). Like $v_{anom_{OLI}}$, this second metric, $v_{anom_{SAR\_day}}$, was calculated using Eq. (3), and all values lying within SAR-derived standard error bounds

($\pm$0.005 m d^{-1}) were discarded during calculation. Upon differencing $v_{anom_{SAR\_day}}$ and $v_{anom_{OLI}}$, we filtered the resulting grid, $v_{anom_{diff}}$, to remove pixels containing unrealistically high values. Visual examination of the raw image data associated with these pixels (not shown) reveal such values to be associated with regions of frequent cloud cover in the Landsat 8 record, which result in more poorly refined velocity estimates with a high standard error. For this purpose, we discarded all instances of $v_{anom_{diff}}$ with a combined error surpassing 0.034 m d^{-1} (12.5 m yr^{-1}), calculated from the mean standard errors associated with our SAR- and optically derived datasets summed in quadrature. Finally, we culled all pixels located within 10 km of the ice divide (where signal-to-noise is often poor using offset tracking techniques; Mouginot et al. (2012)), across regions of complex topography (>15° slope) and near-stagnant (<0.013 m d^{-1}) flow as defined by, respectively, REMA DEM (Howat et al., 2019) and an independent velocity dataset (Rignot et al., 2017) (Fig. 2). All remaining, valid pixels were then used to produce an interpolated heatmap emphasising the spatial coherence of seasonal ice-flow speedup observed in both our SAR- and optically derived velocity records.

4. Results

4.1 GVIIS' grounding line

Our new 2018-2020 grounding line location compilation (cf. Sect. 3.1) provides an important update on GVIIS' geometry, whose only other publicly available InSAR-based records were derived from observations acquired in the mid-1990s (Rignot et al., 2016). In total, our compilation provides revised grounding line information across 76% of GVIIS' coastal margin (Fig. 1). Since the mid-1990s, however, we detect no significant change in grounding line location, with the position of the mid-1990s grounding line falling firmly within the range of tidally induced grounding line locations observed by Sentinel-1A/B (1-5 km depending on the glacier; Fig. B1). In the following sections, all results presented are derived from observations located inland of the high-tide (i.e., most landward) 2018-2020 grounding line location.

4.2 Seasonal ice-flow variability

4.2.1 Spatially resolved patterns of flow

Figures 3 and C1-4 show clear seasonal ice-flow variability along the entire GVIIS coastal margin, with the greatest magnitude of seasonality clustered tightly at or proximal to the deep-bedded grounding lines of the fastest-flowing outlet glaciers (cf. Fig. 1). Along both the Alexander Island and Palmer Land coasts, our calculation of v_{time} (i.e., the month of maximum velocity; cf. Sect. 3.3.1) reveals the ubiquitous occurrence of ice-flow speedup during austral summertime months (DJF; Figs. 3(a) and C1-4(a)). This phenomenon is mirrored in our calculation of $v_{anom_{SAR}}$ (Figs. 3(b) and C1-4(b)), which provides a quantitative measure of the observed ice-flow speedup. For 33% of the outlet glaciers numbered in Fig. 1, observed summertime velocities are $\geq$0.1 m d^{-1} (36.5 m yr^{-1}) faster than the median velocity of all non-summertime seasons, and summertime velocity increases

near the grounding line of all (100%) glaciers exceed error bounds (0.005 m d^{-1} (1.8 m yr^{-1})). Notably, no coherent seasonal signal exists beyond ~10-20 km of the grounding line.

245
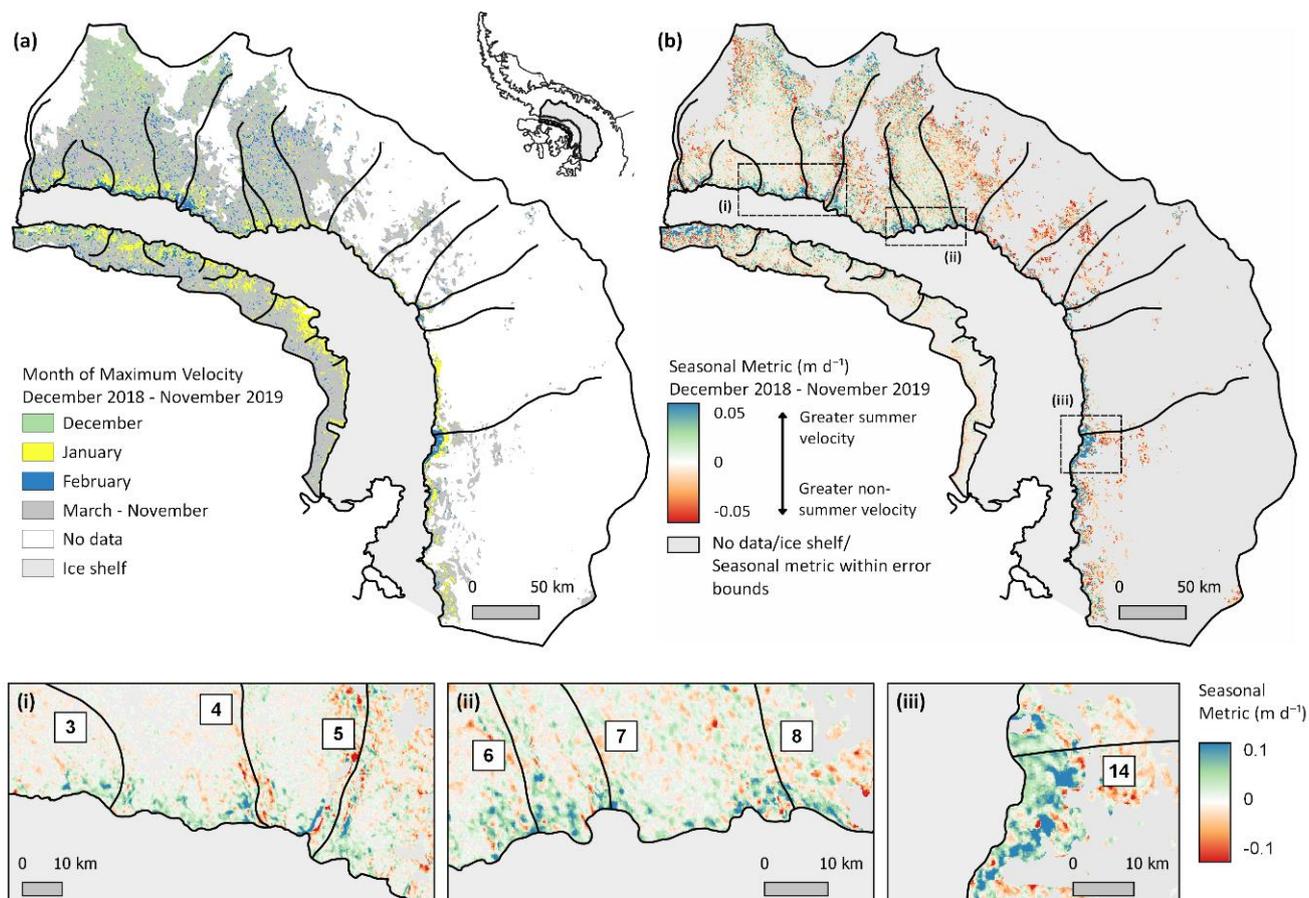
Figure 3 – Spatially resolved patterns of seasonal ice-flow as observed between December 2018 and November 2019. (*a*) shows the month of maximum velocity (v_{time}); (*b*) the calculated velocity anomaly ($v_{anom_{SAR}}$). In (*b*), positive velocity anomalies (blue) indicate summertime speed-up; negative (red), greater velocity during non-summertime months. Dashed boxes denote the location of the inset boxes (*i-iii*). See also Figs. C1-C4.

250

4.2.2 Temporal flow variability near the grounding line

Near the modern-day grounding line, spatially averaged observations of detrended, monthly ice-flow between 2014 and 2020 are consistent with the seasonal signals discussed above (Figs. 3 and C1-4). There, 94% of the outlet glaciers underwent an average summertime (DJF) speedup of 0.06 m d^{-1} (min. 0.02 m d^{-1}; max. 0.15 m d^{-1}; 1σ = 0.037 m d^{-1}), or 21.9 m yr^{-1} (Figs. 4 and A2). This corresponds to, on average, a ~15% summertime increase in ice-flow relative to baseline (timeseries-averaged)

255

rates of ice flow along GVIIS' grounding line. Furthermore, our observations show that 88% of the glaciers underwent velocity minima (blue in Fig. 4) during non-summertime months, and the error bounds associated with all velocity minima fell firmly outside those corresponding to velocity maxima (red in Fig. 4). These seasonal signals are also reflected clearly in our raw

260   (non-detrended) velocity timeseries presented in Fig. A1. Of the velocity profiles shown in Fig. 4, the only glaciers opposing this general pattern were those corresponding to Flowlines 8 (Goodenough Glacier 1) and 10 (unnamed), which exhibit a bimodal and non-summertime speedup signal, respectively. The double peak associated with Flowline 8 is attributed to an anomalous and unexplained regional wintertime speedup in 2016 which dominated the mean velocity signal of this glacier.
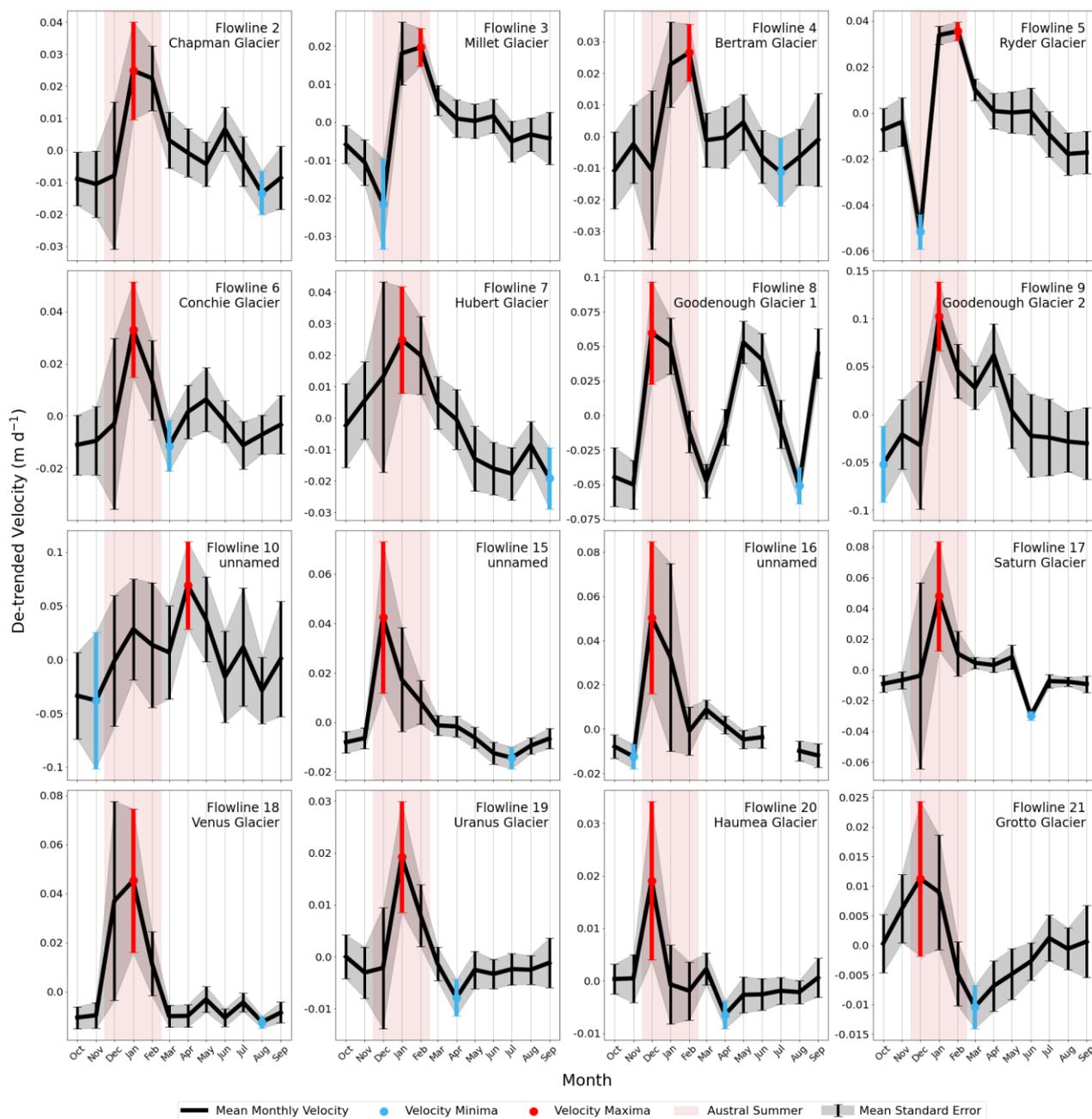
Figure 4 – Detrended SAR-derived observations of mean monthly ice flow between 2014 and 2020 (black) and associated standard error (grey shading). Observations are averaged across the 10 km² dashed boxes shown in Fig. 1. Blue and red error bounds denote velocity minima and maxima, respectively. Translucent red shading denotes the timing of austral summertime (December-February, inclusive). Note that the y-axis limits vary between panels.

270   Spatially, our results are also suggestive of an apparent regional contrast in the timing of summertime speedup, whereby the glaciers nourishing GVIIS from Alexander Island appear to have accelerated in early-to-mid summertime (December – January) compared to those draining from Palmer Land (mid-to-late summertime/autumn (January – April)) (Fig. 5). This finding is also consistent with the approximate timing of peak velocity as determined from discrete Fourier transform analysis (Appendix D). Similar to Fig. 4, this analysis also reveals that most (88%) outlet glaciers have a dominant intra-annual signal

275   characterised by a cosine wave with a frequency of 1 month, implying one complete seasonal cycle per 12-month period (Fig. D1).
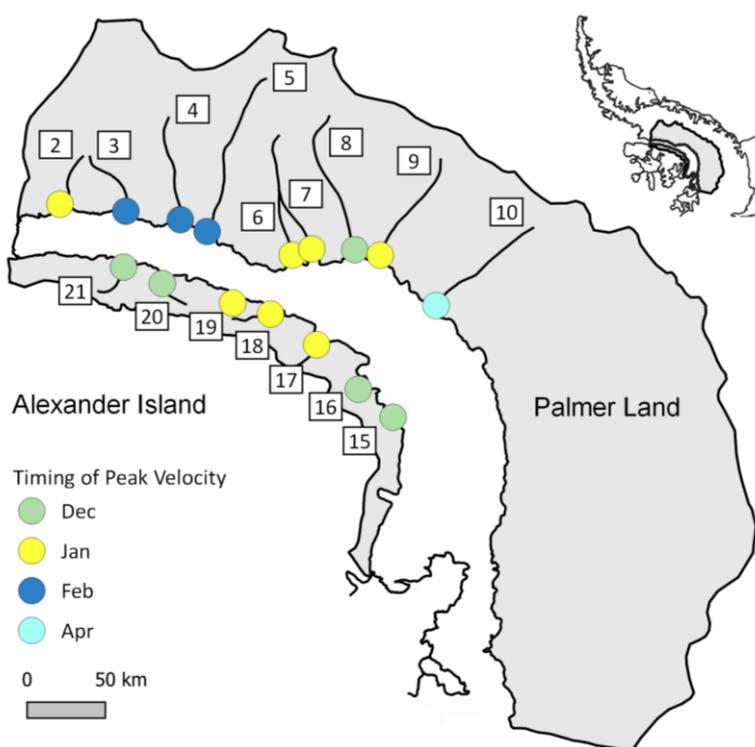
Figure 5 - Month of maximum velocity obtained from the detrended SAR-derived observations shown in Fig. 4. Inset map shows the
280   **location of GVIIS' drainage basins.**

4.2.3 SAR vs. Optical observations of flow

Figure 6 reveals strong agreement between our SAR- and optically derived seasonal observations (i.e., $v_{anom_{SAR\_day}}$ and $v_{anom_{OLI}}$, cf. Sect. 3.3.3), whereby summertime speedups are observed in both datasets within ~10-20 kilometres of the

285   grounding line. There, coincident Sentinel-1-/Landsat 8-derived speedup observations are tightly clustered and confined to the

lateral dimensions of the fast-flowing outlet glaciers (contours in Fig. 6). Farther inland (~40-150+ km from the grounding line), clustered regions of agreement are believed to result from artefacts associated with the interpolation strategy employed during the production of Fig 6, as well as falsely identified regions of speedup falling close to combined sensor error limits (cf. Sect. 3.3.3). Examination of the velocity field (Fig. 1) in conjunction with the phenomena observed in Fig. 6 supports this

290 interpretation, with clustering residing mostly over areas of near-stagnant flow unlikely to have experienced significant seasonal variability (~10 m yr^{-1}). In the few instances where such phenomena are located over regions of faster flow, the spatial distribution of clustering is not bound to the dimensions of the tributary glaciers shown in Figs. 1 and 6, and so is assumed also not to represent a true geophysical signal.
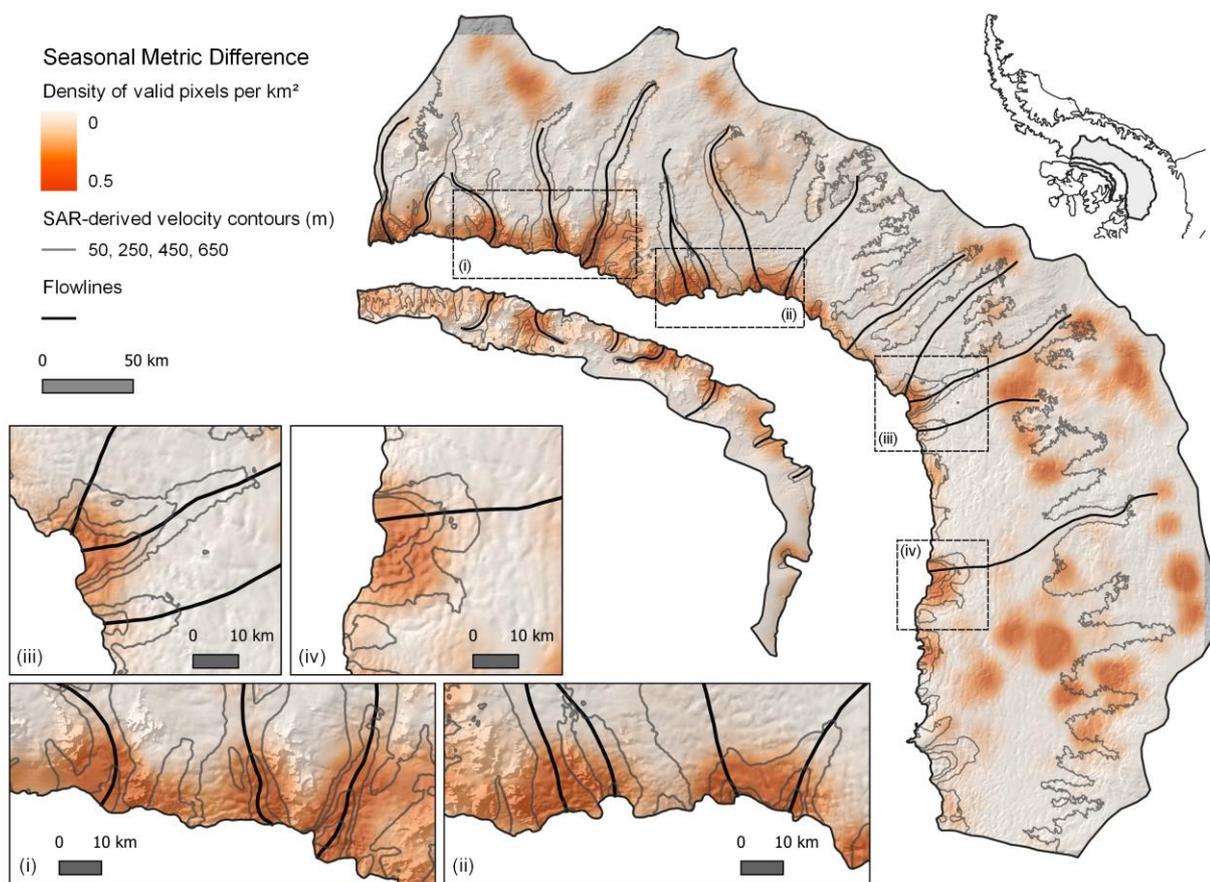
295

Figure 6 - Heatmap indicating the spatial coherence of seasonal ice-flow variability observed by both SAR and optical imaging techniques. Warmer colours denote a higher density (per km^2) of pixels having undergone speedup of comparable magnitude (±10 m yr^{-1}) during austral summertime, as observed in both our SAR- ($v_{anom_{SAR\_day}}$) and optically derived ($v_{anom_{OLI}}$) records (cf. Sect. 3.3.3). Contours are derived from our SAR-derived, timeseries-averaged velocity observations (Sect. 3.2). Background DEM is

300 **derived from the Reference Elevation Model of Antarctica (Howat et al., 2019). Dashed boxes denote the location of the inset boxes (i-iv). Inset map shows the location of GVIIS' drainage basins.**

5. Discussion

Our observations present unambiguous evidence for seasonal ice-flow variability on the grounded ice draining to GVIIS. Proximal to the grounding line, glacier velocity increased during the summertime months (December – February) by $0.06 \pm$
305 0.005 m d^{-1} on average, constituting a ~15% speedup relative to baseline (timeseries-averaged) velocities. In the following sections, we discuss the potential forcing mechanisms driving this phenomenon, which is important, ultimately, for better understanding the future timing and evolution of the Antarctic Ice Sheet's demise.

5.1 Surface forcing

The role of surface-sourced meltwater in stimulating seasonal accelerations in land ice flow is well established on valley
310 glaciers (Iken et al, 1983; Hooke et al, 1989) and the Greenland Ice Sheet (Zwally et al., 2002; Hoffman and Price, 2014; Moon et al., 2014). At both locations, early summertime surface water inputs to a subglacial drainage system drive reductions in effective pressure and increases in basal sliding (Iken, 1981; Schoof, 2010). On the Greenland Ice Sheet, water inputs may be facilitated by hydrofracture associated with rapid supraglacial lake drainage (Tedesco et al, 2013; Stevens et al, 2015). Whilst satellite imaging has documented such drainage events across the Greenland Ice Sheet (Box and Ski, 2007; Selmes et al, 2011),
315 there are only limited observations of supraglacial melting inland of Antarctica's grounding zone (Trusel et al., 2013; Bell et al, 2018). Furthermore, evidence for rapid supraglacial lake drainage events in Antarctica is limited to observations over floating ice only (Langley et al, 2016; Dunmire et al, 2020; Leeson et al, 2020), and no compelling, direct observations of lake drainage exist inland of the grounding zone to date (Rott et al., 2020). Over the observational period of this study (2014-2020), a lack of surface meltwater over grounded ice is consistent with a previously documented, pervasive cooling of the Antarctic
320 Peninsula since the late-1990s (Turner et al., 2016; Adusumilli et al., 2018), and a corresponding reduction in supraglacial melt over most of this time at, and immediately inland of, GVIIS (Banwell et al., 2021). Collectively, these findings imply that surface meltwater-related processes did not drive the summertime speedup signals we observe.

5.2 Ocean forcing

In the absence of any surface-related forcing (cf. Sect. 5.1), the clear seasonal velocity signals we observe (Figs. 3 and 4) are
325 suggestive of an oceanic influence. This interpretation is supported by in situ oceanographic observations revealing the widespread inflow and flooding of almost unmodified, relatively warm CDW to GVIIS' cavity, which is sourced from the continental shelf via a net northwards throughflow from Ronne Entrance (Jenkins and Jacobs, 2008; Meredith et al., 2010). There, the strongest inflows of CDW have been observed to occur underneath its northern margin proximal to Alexander Island (red arrow in Fig. 1; after Jenkins and Jacobs, 2008), which may explain the observed, earlier onset of summertime speedup
330 along that stretch of coastline relative to Palmer Land (Fig. 5). We further expect that enhanced CDW upwelling in the cavity, enabled by the buoyancy driven advection of ice-shelf meltwater entrained within the northerly throughflow and deflected towards Alexander Island due to Coriolis forcing, will have maximised this contrasting regional melting effect. This hypothesis

is consistent with in situ- and modelling-based estimates of GVIIS' sub-shelf circulation (Jenkins and Jacobs, 2008; Holland et al., 2010) and, more broadly, with inferred patterns of recently observed melting along the Coriolis-favoured flank of Dotson

335 Ice Shelf, West Antarctica (Gourmelen et al., 2017).

Across GVIIS more generally, the ubiquitous speedup signals we observe are likely related to seasonal fluctuations in CDW forcing. Indeed, recent research has revealed two possible mechanisms in which sea ice conditions offshore from GVIIS may control CDW draft in its sub-shelf cavity. First, modelling studies have suggested a process of wintertime sea-ice growth, brine

340 rejection and resulting convection throughout the mixed layer that leads to a thickening of the underlying CDW (Holland et al., 2010; Meredith et al., 2010; Petty et al., 2014). These processes are believed to drive a seasonal cycle in melt rate at GVIIS' grounding line (Holland et al., 2010), greatest around mid-to-late wintertime, which precedes the resulting summertime accelerations in ice flow we observe by ~3-5 months. Several ice-sheet modelling studies have suggested a lag time of weeks to months from the onset of ocean-induced melt to ice acceleration at the grounding line (Vieli and Nick, 2011; Joughin et al.,

345 2012b), suggesting that this timescale is reasonable. Alternatively, limited in situ observations from the Amundsen Sea Sector have revealed that sea-ice growth and associated brine rejection can result in a destratification of the water column and thus restrict CDW inflow during austral wintertime (Webber et al., 2017). This mechanism would, by implication, facilitate enhanced melt at the grounding line more in-phase with the summertime accelerations in ice flow we observe. Compared to the relatively well-understood ice-ocean interactions at work in Amundsen Sea Sector, however, a historical dearth of

350 oceanographic observations in the Bellingshausen Sea hinders our ability to ascertain which mechanism is the dominant control on CDW influx to GVIIS' sub-shelf cavity, justifying the future collection of detailed oceanographic data in this region. Beyond relatively local-scale, seasonal variations in ocean forcing, modelling experiments further suggest that CDW transport to GVIIS' cavity is relatively insensitive to far-field intra-annual-to-decadal-scale atmosphere-ocean variability (Holland et al., 2010). Notably, this lies in contrast to the atmosphere-ocean processes controlling CDW transmission to the Amundsen

355 coastal margin (Steig et al., 2012; Dutrieux et al., 2014; Jenkins et al., 2018; Paolo et al. 2018), further implicating sea-ice induced oceanographic modification as the key control on the seasonal velocity signals we observe at GVIIS.

6. Summary and Implications

We provide the first evidence for seasonal flow variability of land ice draining to George VI Ice Shelf (GVIIS). Using monthly Sentinel-1 SAR-based velocity information derived from high-frequency (6-/12-day) repeat-pass observations, we detect a

360 ~15% mean austral summertime speedup of the outlet glaciers feeding GVIIS at, and immediately inland of, the grounding line. This seasonal variability is corroborated by independent, optically derived observations of ice flow. Regional contrasts in the onset of ice-flow acceleration and the overall timing of the speedup events across GVIIS fingerprint oceanic forcing as the primary control of this seasonality. Overall, our findings imply that other glaciers in Antarctica may be susceptible to — and currently undergoing — similar ocean-driven ice flow seasonality, especially those fronted by warm-based, CDW-laden ice-

365   shelf cavities including the highly vulnerable and rapidly retreating Pine Island and Thwaites glaciers. Ascertaining the nature

of seasonal ice-ocean interactions at such locations is important, therefore, for better understanding, modelling, and ultimately

refining projections of the rate at which future Antarctic ice-losses will contribute to global sea-level rise.

Appendices

Appendix A
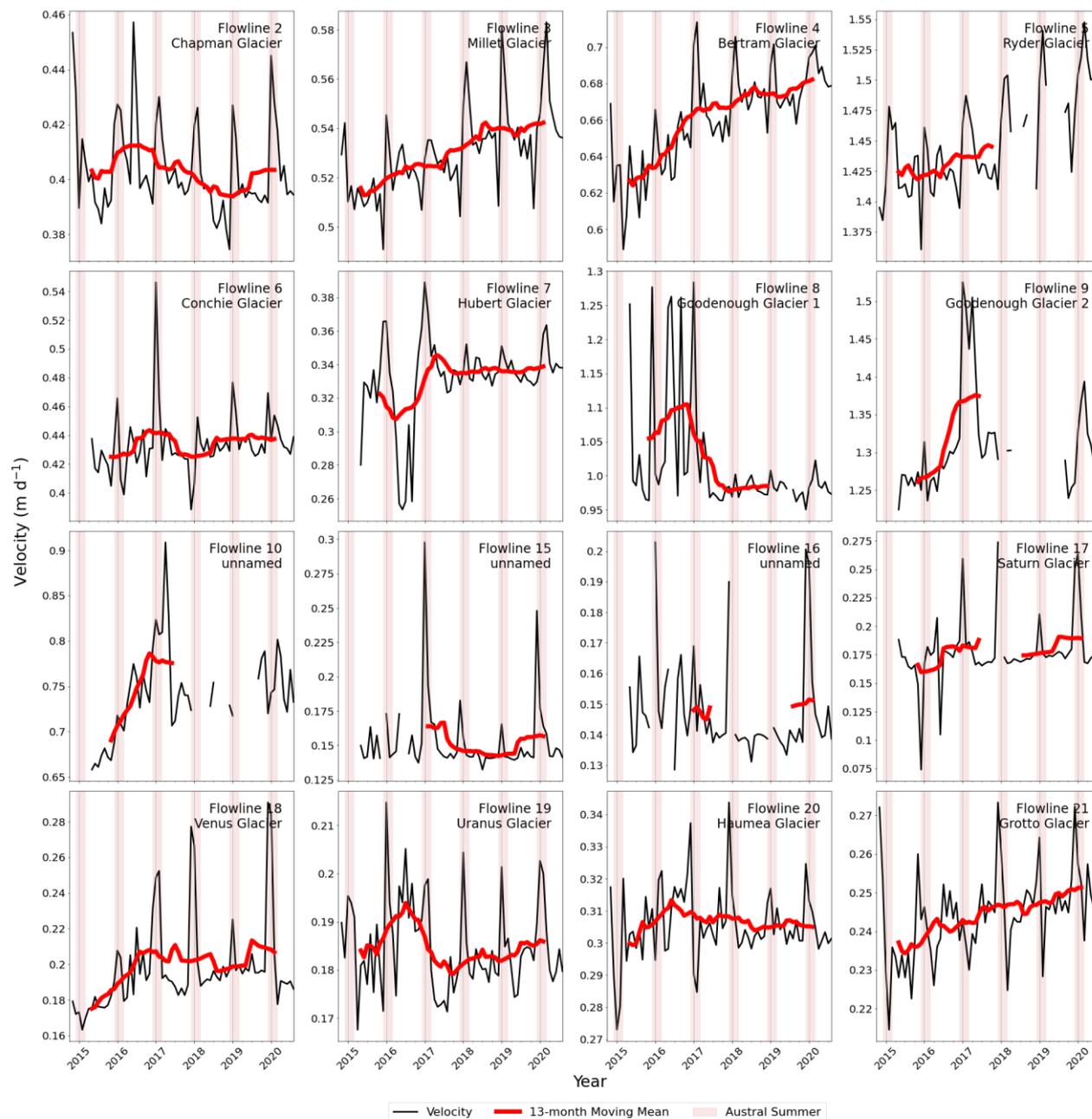
370

Figure A1 - SAR-derived observations of ice flow for each month between October 2014 and August 2020 (black line) and the 13-month moving mean ice flow (red line). Observations are averaged across the 10 km^2 dashed boxes shown in Fig. 1. Translucent red shading denotes the timing of austral summertime (December–February, inclusive). Note that the y-axis limits vary between panels.
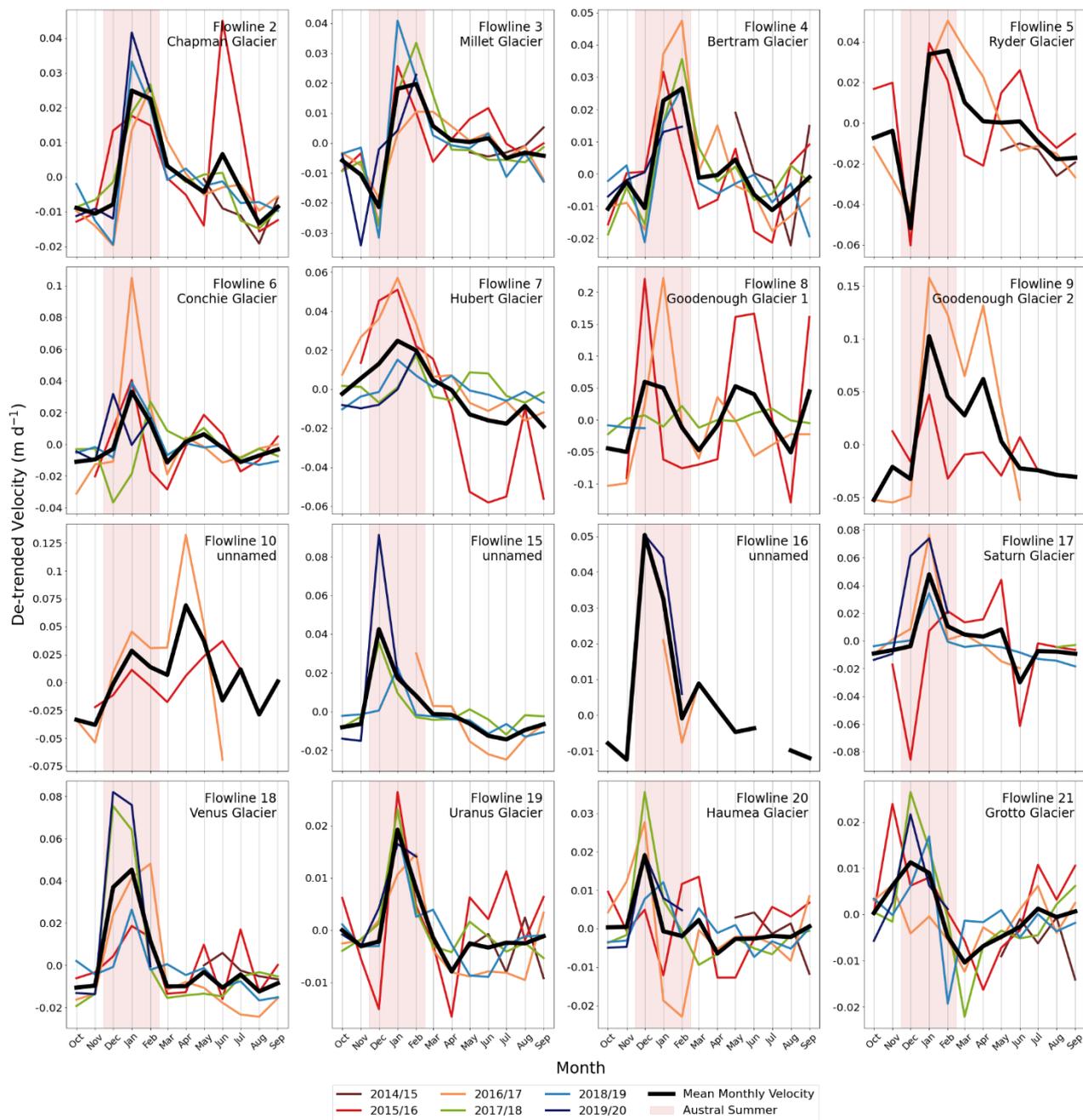
Figure A2 - Detrended SAR-derived observations of mean monthly ice flow for each year between 2014 and 2020 (coloured lines) and the mean monthly ice flow calculated over the entire time series (black line; same as Fig. 4). Observations are averaged across the 10 km² dashed boxes shown in Fig. 1. Translucent red shading denotes the timing of austral summertime (December–February, inclusive). Note that the y-axis limits vary between panels.

380 **Appendix B**
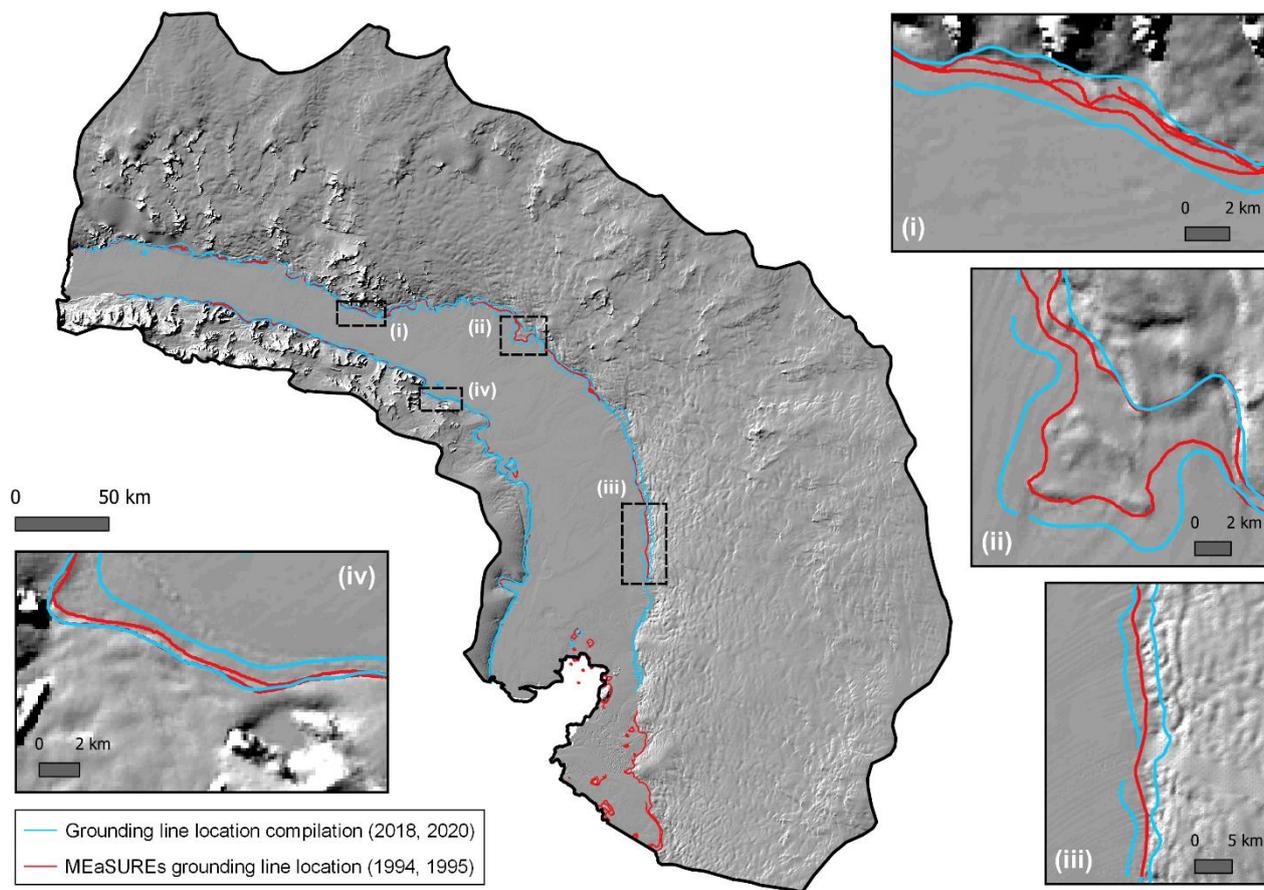
Figure B1 - Landward (high-tide) and seaward (low-tide) limits of the modern-day (2018-2020) grounding line (blue) and the position of the grounding line in the mid-1990s (red). Background hillshade is derived from the Reference Elevation Model of Antarctica (Howat et al., 2019). Dashed boxes denote the location of the inset boxes (*i-iv*).
385 **Appendix C**
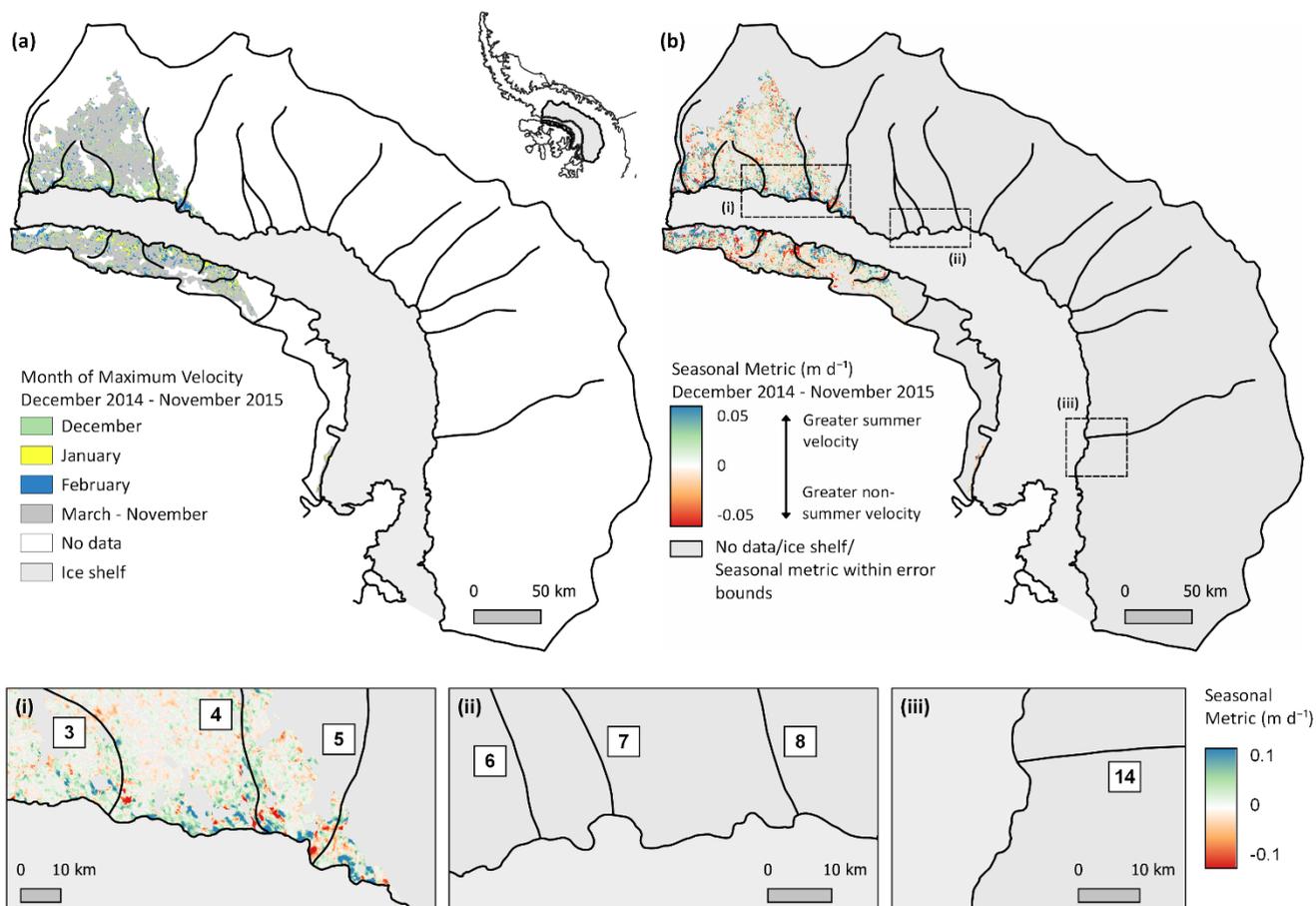
Figure C1 - Same as Fig. 3 but showing spatially resolved patterns of seasonal ice-flow as observed between December 2014 and November 2015. (a) shows the month of maximum velocity (v_{time}); (b) the calculated velocity anomaly ($v_{anom_{SAR}}$). In (b), positive velocity anomalies (blue) indicate summertime speed-up; negative (red), greater velocity during non-summertime months. Dashed boxes denote the location of the inset boxes (*i-iii*). Note that insets ii and iii contain no data for the period December 2014-November 390 2015. See also Figs. C2-C4.
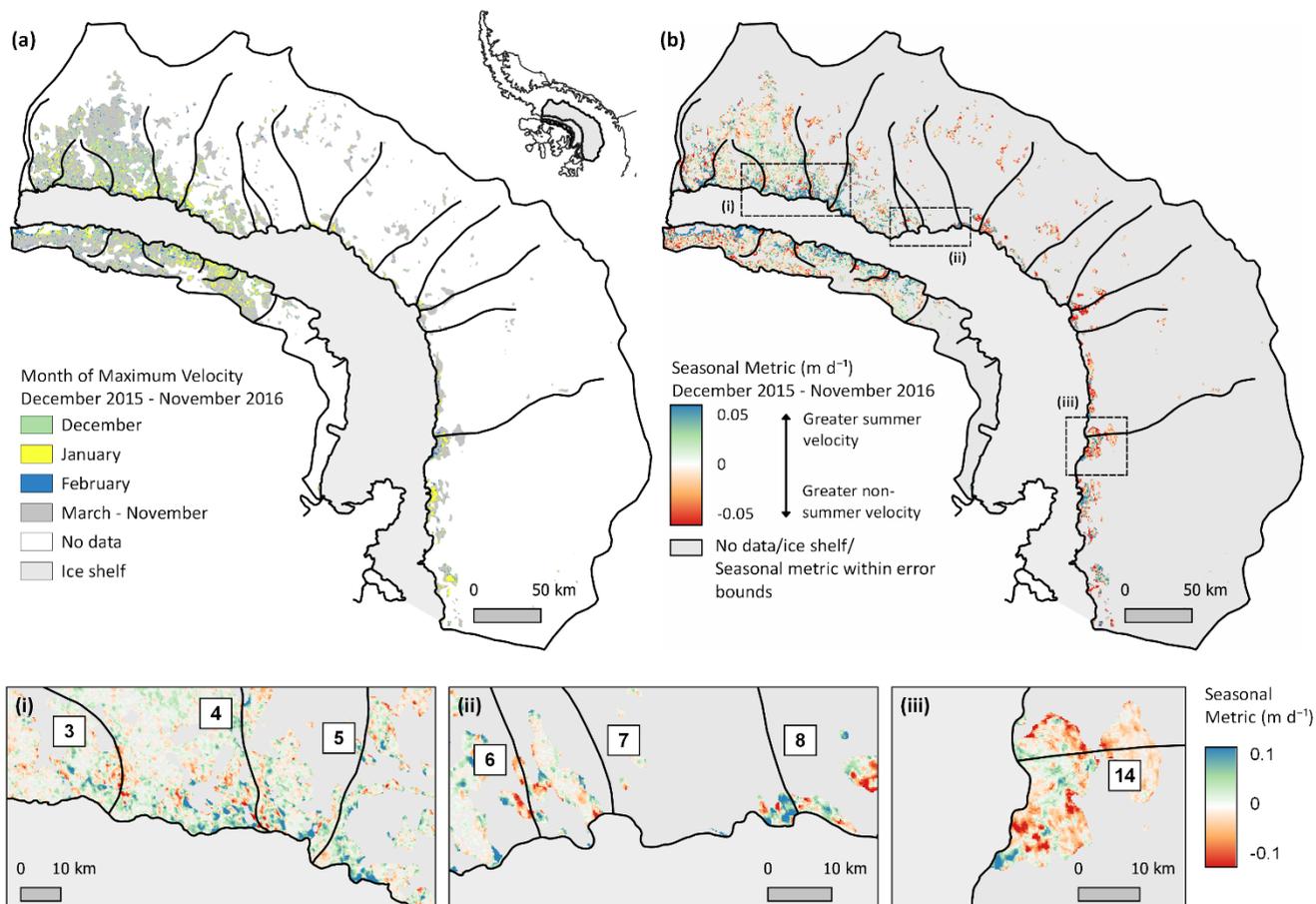
Figure C2 - Same as Fig. 3 but showing spatially resolved patterns of seasonal ice-flow as observed between December 2015 and November 2016. (a) shows the month of maximum velocity (v_{time}); (b) the calculated velocity anomaly ($v_{anom_{SAR}}$). In (b), positive velocity anomalies (blue) indicate summertime speed-up; negative (red), greater velocity during non-summertime months. Dashed boxes denote the location of the inset boxes (*i-iii*). See also Figs. C1, C3-C4.
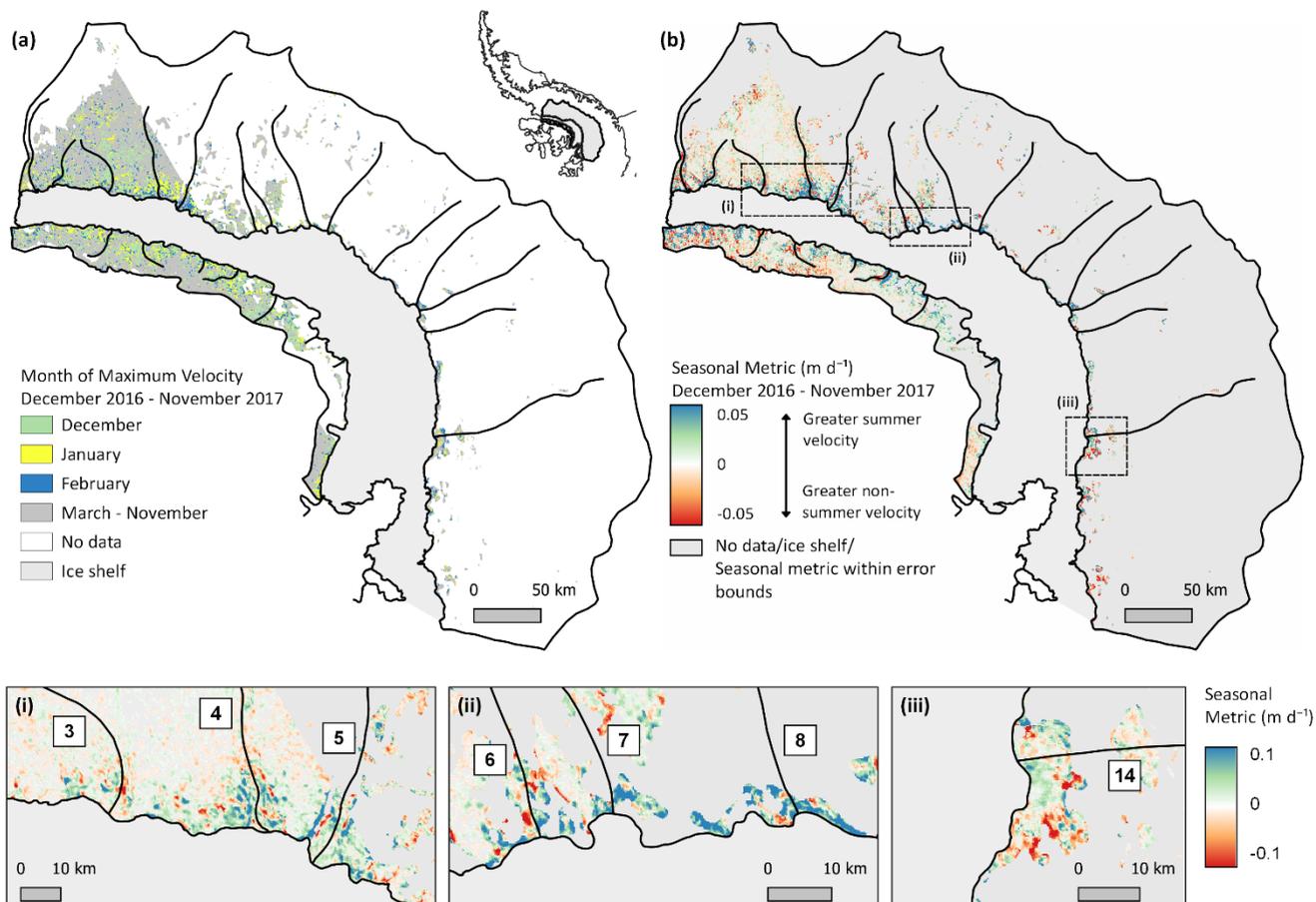
Figure C3 - Same as Fig. 3 but showing spatially resolved patterns of seasonal ice-flow as observed between December 2016 and November 2017. (a) shows the month of maximum velocity (v_{time}); (b) the calculated velocity anomaly ($v_{anom_{SAR}}$). In (b), positive velocity anomalies (blue) indicate summertime speed-up; negative (red), greater velocity during non-summertime months. Dashed boxes denote the location of the inset boxes (*i-iii*). See also Figs. C1-C2 and C4.

400
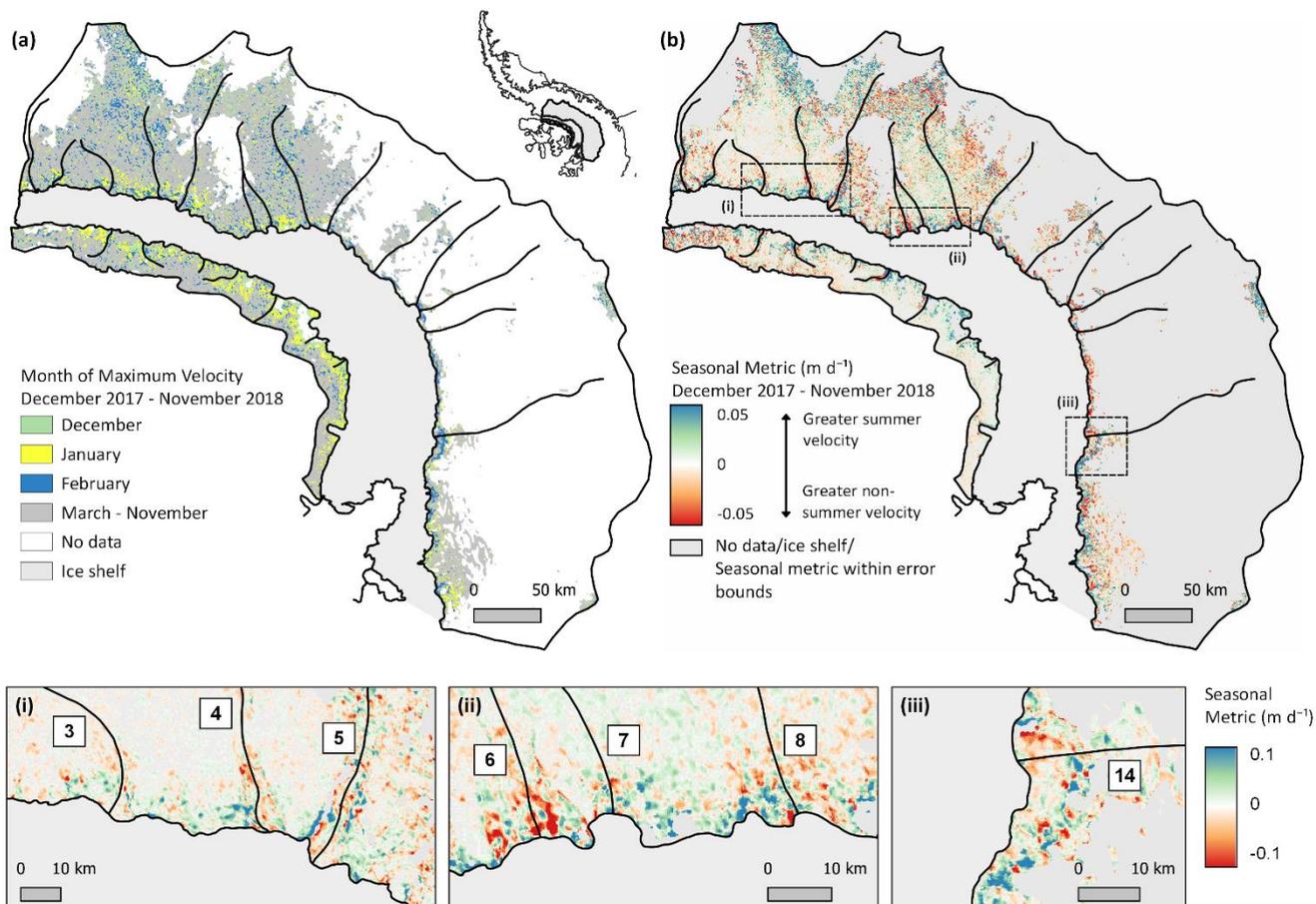
Figure C4 - Same as Fig. 3 but showing spatially resolved patterns of seasonal ice-flow as observed between December 2017 and November 2018. (a) shows the month of maximum velocity (v_{time}); (b) the calculated velocity anomaly ($v_{anom_{SAR}}$). In (b), positive velocity anomalies (blue) indicate summertime speed-up; negative (red), greater velocity during non-summertime months. Dashed boxes denote the location of the inset boxes (*i-iii*). See also Figs. C1-C3.

Appendix D

For most of the outlet glaciers numbered in Figs. A2 and D1, the modelled timing of peak velocity (Table D1) does not align precisely with the month of maximum velocity established from observations (Figs. 4 and 5). To model peak velocity timing,
415 a cosine wave, optimised to the most dominant frequency observed across all outlet glacier time series (1 month), is fitted to each time series (Fig. D1, left hand panels). The modelled results are subsequently calculated from the phase shift of each fitted cosine wave (Table D1); as such, the modelled timing of peak velocity should be considered a broad-brush indicator of the approximate timing only. The most dominant frequency present in the original function, however, is derived directly from the discrete Fourier transform (Fig. D1, right hand panels), and hence presents meaningful information on the seasonality of
420 each timeseries.

Figure D1 - Discrete Fourier transform outputs. Left hand panels indicate the time domain where time 0 denotes 1st October. Panels show mean monthly ice flow of each outlet glacier (blue; same as Fig. 4) with fitted cosine functions (orange) optimised to the most dominant frequency observed across all outlet glacier time series. Right hand panels indicate the frequency domain, whereby the greatest amplitude associated with each glacier timeseries denotes the most dominant frequency. In the context of the present study, a dominant frequency of 1 denotes one complete seasonal cycle per year. Annotated values indicate the phase associated with each frequency component.

425

Table D1 - Phase and amplitude characteristics of the fitted cosine function optimised to the dominant frequency determined by discrete Fourier transform analysis (Fig. D1, orange). Flowlines 2-10 drain Palmer Land, while flowlines 15-21 drain Alexander Island.

Flowline	Amplitude (A)	Phase (φ)	Max Occurs (1 Oct + t (months))	Modelled Timing of Peak Velocity[1]	Season of Peak Velocity[1]
2	0.012	-2.35	1 Oct + 4.48	15 February	Late Summer
3	0.009	-2.70	1 Oct + 5.16	5 March	Late Extended Summer
4	0.011	-2.13	1 Oct + 4.07	3 February	Late Summer
5	0.017	-2.58	1 Oct + 4.93	28 February	Late Summer
6	0.010	-2.12	1 Oct + 4.04	2 February	Late Summer
7	0.019	-1.63	1 Oct + 3.10	4 January	Midsummer
8	0.009	-2.97	1 Oct + 5.67	21 March	Late Extended Summer
9	0.050	-2.42	1 Oct + 4.63	19 February	Late Summer
10	0.032	-2.97	1 Oct + 5.68	21 March	Late Extended Summer
15	0.016	-1.49	1 Oct + 2.85	26 December	Early Summer
16	0.017	-1.69	1 Oct + 3.23	7 January	Midsummer
17	0.016	-1.91	1 Oct + 3.66	20 January	Midsummer
18	0.018	-1.51	1 Oct + 2.88	27 December	Early Summer
19	0.005	-1.48	1 Oct + 2.82	25 December	Early Summer
20	0.005	-0.88	1 Oct + 1.68	21 November	Early Extended Summer
21	0.006	-0.43	1 Oct + 0.82	25 October	Early Extended Summer

[1]Note: The modelled timing of peak velocity is derived from the phase value associated with each of the numbered outlet glaciers.

Data Availability

All grounding line and velocity datasets presented in this study are available at https://doi.org/10.17863/CAM.82248 and
435   https://doi.org/10.17863/CAM.82252, respectively (Boxall et al., 2022a; 2022b). Copernicus Sentinel-1A/B data used in this
study are available from the European Space Agency at https://scihub.copernicus.eu/; Landsat 8 ITS_LIVE velocity data
(Gardner et al., 2019) are available from https://its-live.jpl.nasa.gov/; annual MEaSUREs Antarctic ice velocity maps (Rignot
et al., 2017) are available from the National Snow and Ice Data Center (NSIDC) at https://nsidc.org/data/NSIDC-
0720/versions/1; REMA DEM (Howat et al., 2019) is publicly available at https://www.pgc.umn.edu/data/rema/, and the 2018
440   grounding line position (Mohajerani et al., 2021) is available at https://doi.org/10.7280/D1VD6G.

Author Contributions

KB designed the study under the supervision of FDWC and ICW. JW and TN processed the monthly composite SAR-derived
velocity grids. KB performed all analyses. KB wrote the manuscript under the guidance of FDWC, with contributions from all
co-authors.

445   ## Competing Interests

The authors declare that they have no conflict of interest.

Acknowledgments

This research was undertaken while KB was in receipt of a United Kingdom Natural Environment Research Council PhD
studentship awarded through the University of Cambridge C-CLEAR Doctoral Training Partnership (grant number:
450   NE/S007164/1). This work was also produced with financial assistance (to FDWC) of the Prince Albert II of Monaco
Foundation, and (to ICW) from the United Kingdom Natural Environment Research Council awarded to the University of
Cambridge (grant number: NE/T006234/1). TN and JW acknowledge support from the European Space Agency through the
Antarctic Ice Sheet Climate Change Initiative (CCI) program. The authors wish to thank W.G. Rees for his advice regarding
the discrete Fourier transform analyses presented in the manuscript.

455   ## References

Adusumilli, S., Fricker, H.A., Siegfried, M.R., Padman, L., Paolo, F.S., Ligtenberg, S.R.M., 2018. Variable Basal Melt Rates
of Antarctic Peninsula Ice Shelves, 1994–2016. *Geophys. Res. Lett. 45*, 4086–4095.
https://doi.org/10.1002/2017GL076652

Banwell, A.F., MacAyeal, D.R. and Sergienko, O.V., 2013. Breakup of the Larsen B Ice Shelf triggered by chain reaction
460   drainage   of   supraglacial   lakes. *Geophysical   Research   Letters*, 40(22),   pp.5872-5876.
         https://doi.org/10.1002/2013GL057694

Banwell, A.F., Datta, R.T., Dell, R.L., Moussavi, M., Brucker, L., Picard, G., Shuman, C.A., Stevens, L.A., 2021. The 32-year
         record-high surface melt in 2019/2020 on the northern George VI Ice Shelf, Antarctic Peninsula. *The Cryosphere 15*,
         909–925. https://doi.org/10.5194/tc-15-909-2021

465 Bell, R.E., Banwell, A.F., Trusel, L.D. and Kingslake, J., 2018. Antarctic surface hydrology and impacts on ice-sheet mass
         balance. *Nature Climate Change, 8*(12), pp.1044-1052. https://doi.org/10.1038/s41558-018-0326-3

Box, J.E., Ski, K., 2007. Remote sounding of Greenland supraglacial melt lakes: implications for subglacial hydraulics. *J.*
         Glaciol. 53, 257–265. https://doi.org/10.3189/172756507782202883

Boxall, K., Christie, F.D.W., Willis, I.C., Wuite, J. And Nagler, T. 2022a. West Antarctic Peninsula grounding line location
470   datasets   supporting   "Seasonal   land   ice-flow   variability   in   the   Antarctic   Peninsula".   [Dataset]
         https://doi.org/10.17863/CAM.82248

Boxall, K., Christie, F.D.W., Willis, I.C., Wuite, J. And Nagler, T. 2022b. West Antarctic Peninsula seasonal ice velocity
         products   supporting   "Seasonal   land   ice-flow   variability   in   the   Antarctic   Peninsula".   [Dataset]
         https://doi.org/10.17863/CAM.82252

475 Bracewell, R., 1978. The Fourier transform and its applications. McGraw-Hill, Inc., New York.

Christie, F.D.W., Bingham, R.G., Gourmelen, N., Steig, E.J., Bisset, R.R., Pritchard, H.D., Snow, K., Tett, S.F.B., 2018.
         Glacier change along West Antarctica's Marie Byrd Land Sector and links to inter-decadal atmosphere–ocean
         variability. *The Cryosphere 12*, 2461–2479. https://doi.org/10.5194/tc-12-2461-2018

Christie, F.D.W., Bingham, R.G., Gourmelen, N., Tett, S.F.B., Muto, A., 2016. Four-decade record of pervasive grounding
480   line retreat along the Bellingshausen margin of West Antarctica. *Geophys. Res. Lett. 43*, 5741–5749.
         https://doi.org/10.1002/2016GL068972

Dirscherl, M. C., Dietz, A. J., and Kuenzer, C., 2021. Seasonal evolution of Antarctic supraglacial lakes in 2015–2021 and
         links to environmental controls. *The Cryosphere*, 15, 5205–5226, https://doi.org/10.5194/tc-15-5205-2021

Dunmire, D., Lenaerts, J.T.M., Banwell, A.F., Wever, N., Shragge, J., Lhermitte, S., Drews, R., Pattyn, F., Hansen, J.S.S.,
485   Willis, I.C. and Miller, J., 2020. Observations of buried lake drainage on the Antarctic Ice Sheet. *Geophysical*
         Research Letters, 47(15), p.e2020GL087970. https://doi.org/10.1029/2020GL087970

Dutrieux, P., Rydt, J.D., Jenkins, A., Holland, P.R., Ha, H.K., Lee, S.H., Steig, E.J., Ding, Q., Abrahamsen, E.P., Schröder,
         M., 2014. Strong Sensitivity of Pine Island Ice-Shelf Melting to Climatic Variability. *Science 343*, 174–178.
         https://doi.org/10.1126/science.1244341

490 Edwards, T.L., Nowicki, S., Marzeion, B., Hock, R., Goelzer, H., Seroussi, H., Jourdain, N.C., Slater, D.A., Turner, F.E.,
         Smith, C.J., McKenna, C.M., Simon, E., Abe-Ouchi, A., Gregory, J.M., Larour, E., Lipscomb, W.H., Payne, A.J.,
         Shepherd, A., Agosta, C., Alexander, P., Albrecht, T., Anderson, B., Asay-Davis, X., Aschwanden, A., Barthel, A.,

Bliss, A., Calov, R., Chambers, C., Champollion, N., Choi, Y., Cullather, R., Cuzzone, J., Dumas, C., Felikson, D., Fettweis, X., Fujita, K., Galton-Fenzi, B.K., Gladstone, R., Golledge, N.R., Greve, R., Hattermann, T., Hoffman, M.J., Humbert, A., Huss, M., Huybrechts, P., Immerzeel, W., Kleiner, T., Kraaijenbrink, P., Le Clec'h, S., Lee, V., Leguy, G.R., Little, C.M., Lowry, D.P., Malles, J.-H., Martin, D.F., Maussion, F., Morlighem, M., O'Neill, J.F., Nias, I., Pattyn, F., Pelle, T., Price, S.F., Quiquet, A., Radić, V., Reese, R., Rounce, D.R., Rückamp, M., Sakai, A., Shafer, C., Schlegel, N.-J., Shannon, S., Smith, R.S., Straneo, F., Sun, S., Tarasov, L., Trusel, L.D., Van Breedam, J., van de Wal, R., van den Broeke, M., Winkelmann, R., Zekollari, H., Zhao, C., Zhang, T., Zwinger, T., 2021. Projected land ice contributions to twenty-first-century sea level rise. *Nature 593*, 74–82. https://doi.org/10.1038/s41586-021-03302-y

ESA, 2022. User Guides - Sentinel-1 SAR - Sentinel Online - Sentinel Online. [online] Available at: <https://sentinel.esa.int/web/sentinel/user-guides/sentinel-1-sar> [Accessed January 2022].

Fricker, H.A., Coleman, R., Padman, L., Scambos, T.A., Bohlander, J., Brunt, K.M., 2009. Mapping the grounding zone of the Amery Ice Shelf, East Antarctica using InSAR, MODIS and ICESat. *Antarct. Sci. 21*, 515–532. https://doi.org/10.1017/S095410200999023X

Friedl, P., Weiser, F., Fluhrer, A., Braun, M.H., 2020. Remote sensing of glacier and ice sheet grounding lines: A review. *Earth-Sci. Rev. 201*, 102948. https://doi.org/10.1016/j.earscirev.2019.102948

Gardner, A. S., M. A. Fahnestock, and T. A. Scambos, 2019 [Accessed January 2022]: MEaSUREs ITS_LIVE Landsat Image-Pair Glacier and Ice Sheet Surface Velocities: Version 1, https://doi.org/10.5067/IMR9D3PEI28U

Gardner, A.S., Moholdt, G., Scambos, T., Fahnstock, M., Ligtenberg, S., Van Den Broeke, M., Nilsson, J., 2018. Increased West Antarctic and unchanged East Antarctic ice discharge over the last 7 years. *The Cryosphere 12*, 521–547. https://doi.org/10.5194/tc-12-521-2018

Gourmelen, N., Goldberg, D.N., Snow, K., Henley, S.F., Bingham, R.G., Kimura, S., Hogg, A.E., Shepherd, A., Mouginot, J., Lenaerts, J.T.M., Ligtenberg, S.R.M., van de Berg, W.J., 2017. Channelized Melting Drives Thinning Under a Rapidly Melting Antarctic Ice Shelf. *Geophys. Res. Lett. 44*, 9796–9804. https://doi.org/10.1002/2017GL074929

Greene, C.A., Young, D.A., Gwyther, D.E., Galton-Fenzi, B.K. and Blankenship, D.D., 2018. Seasonal dynamics of Totten Ice Shelf controlled by sea ice buttressing. *The Cryosphere*, 12(9), pp.2869-2882. https://doi.org/10.5194/tc-12-2869-2018

Hoffman, M., Price, S., 2014. Feedbacks between coupled subglacial hydrology and glacier dynamics. *J. Geophys. Res. Earth Surf. 119*, 414–436. https://doi.org/10.1002/2013JF002943

Hogg, A.E., Shepherd, A., Cornford, S.L., Briggs, K.H., Gourmelen, N., Graham, J.A., Joughin, I., Mouginot, J., Nagler, T., Payne, A.J., Rignot, E., Wuite, J., 2017. Increased ice flow in Western Palmer Land linked to ocean melting. *Geophys. Res. Lett. 44*, 4159–4167. https://doi.org/10.1002/2016GL072110

Holland, P. R., A. Jenkins, and D. M. Holland, 2010, Ice and ocean processes in the Bellingshausen Sea, Antarctica, *J. Geophys. Res.,115*, C05020, https://doi.org/10.1029/2008JC005219

Holt, T.O., Glasser, N.F., Quincey, D.J. and Siegfried, M.R., 2013. Speedup and fracturing of George VI Ice Shelf, Antarctic Peninsula. *The Cryosphere, 7*(3), 797-816. https://doi.org/10.5194/tcd-7-373-2013

Hooke, R.L., Calla, P., Holmlund, P., Nilsson, M. and Stroeven, A., 1989. A 3 year record of seasonal variations in surface velocity, Storglaciären, Sweden. *Journal of Glaciology*, 35(120), pp.235-247. https://doi.org/10.3189/S0022143000004561

Howat, I.M., Porter, C., Smith, B.E., Noh, M.-J., Morin, P., 2019. The Reference Elevation Model of Antarctica. *The Cryosphere 13*, 665–674. https://doi.org/10.5194/tc-13-665-2019

Iken, A., 1981. The effect of the subglacial water pressure on the sliding velocity of a glacier in an idealized numerical model. *Journal of Glaciology*, 27(97), pp.407-421. https://doi.org/10.3189/S0022143000011448

Iken, A., Röthlisberger, H., Flotron, A. and Haeberli, W., 1983. The uplift of Unteraargletscher at the beginning of the melt season—a consequence of water storage at the bed?. *Journal of Glaciology*, 29(101), pp.28-47. https://doi.org/10.3189/S0022143000005128

Jenkins, A., Dutrieux, P., Jacobs, S.S., McPhail, S.D., Perrett, J.R., Webb, A.T., White, D., 2010. Observations beneath Pine Island Glacier in West Antarctica and implications for its retreat. *Nat. Geosci. 3*, 468–472. https://doi.org/10.1038/ngeo890

Jenkins, A., and S. Jacobs, 2008, Circulation and melting beneath George VI Ice Shelf, Antarctica, *J. Geophys. Res.,113*, C04013, https://doi.org/10.1029/2007JC004449

Jenkins, A., Shoosmith, D., Dutrieux, P., Jacobs, S., Kim, T.W., Lee, S.H., Ha, H.K. and Stammerjohn, S., 2018. West Antarctic Ice Sheet retreat in the Amundsen Sea driven by decadal oceanic variability. *Nature Geoscience*, 11(10), pp.733-738. https://doi.org/10.1038/s41561-018-0207-4

Joughin, I., Alley, R.B., Holland, D.M., 2012a. Ice-Sheet Response to Oceanic Forcing. *Science 338*, 1172–1176. https://doi.org/10.1126/science.1226481

Joughin, I., Shean, D.E., Smith, B.E., Dutrieux, P., 2016. Grounding line variability and subglacial lake drainage on Pine Island Glacier, Antarctica. *Geophys. Res. Lett. 43*, 9093–9102. https://doi.org/10.1002/2016GL070259

Joughin, I., B. E. Smith, I. M. Howat, D. Floricioiu, R. B. Alley, M. Truffer, and M. Fahnestock, 2012b, Seasonal to decadal scale variations in the surface velocity of Jakobshavn Isbrae, Greenland: Observation and model-based analysis, *J. Geophys. Res.,117*, F02030, https://doi.org/10.1029/2011JF002110

Joughin, I., Smith, B.E., Howat, I., 2018. Greenland Ice Mapping Project: ice flow velocity variation at sub-monthly to decadal timescales. *The Cryosphere 12*, 2211–2227. https://doi.org/10.5194/tc-12-2211-2018

King, M.D., Howat, I.M., Jeong, S., Noh, M.J., Wouters, B., Noël, B., van den Broeke, M.R., 2018. Seasonal to decadal variability in ice discharge from the Greenland Ice Sheet. *The Cryosphere 12*, 3813–3825. https://doi.org/10.5194/tc-12-3813-2018

Kingslake, J., Ely, J.C., Das, I., Bell, R.E., 2017. Widespread movement of meltwater onto and across Antarctic ice shelves. *Nature 544*, 349–352. https://doi.org/10.1038/nature22049

Konrad, H., Shepherd, A., Gilbert, L., Hogg, A.E., McMillan, M., Muir, A., Slater, T., 2018. Net retreat of Antarctic glacier grounding lines. *Nat. Geosci. 11*, 258–262. https://doi.org/10.1038/s41561-018-0082-z

Langley, E.S., Leeson, A.A., Stokes, C.R. and Jamieson, S.S., 2016. Seasonal evolution of supraglacial lakes on an East Antarctic outlet glacier. *Geophysical Research Letters*, 43(16), pp.8563-8571. https://doi.org/10.1002/2016GL069511

Leeson, A.A., Forster, E., Rice, A., Gourmelen, N. and Van Wessem, J.M., 2020. Evolution of supraglacial lakes on the Larsen B ice shelf in the decades before it collapsed. *Geophysical Research Letters, 47*(4), p.e2019GL085591. https://doi.org/10.1029/2019GL085591

Meredith, M.P., Wallace, M.I., Stammerjohn, S.E., Renfrew, I.A., Clarke, A., Venables, H.J., Shoosmith, D.R., Souster, T., Leng, M.J., 2010. Changes in the freshwater composition of the upper ocean west of the Antarctic Peninsula during the first decade of the 21st century. Prog. Oceanogr., 3rd GLOBEC OSM: From ecosystem function to ecosystem prediction 87, 127–143. https://doi.org/10.1016/j.pocean.2010.09.019

Mohajerani, Y., Jeong, S., Scheuchl, B., Velicogna, I., Rignot, E., Milillo, P., 2021. Automatic delineation of glacier grounding lines in differential interferometric synthetic-aperture radar data using deep learning. *Sci. Rep. 11*, 4992. https://doi.org/10.1038/s41598-021-84309-3

Moon, T., Joughin, I., Smith, B., Van Den Broeke, M.R., Van De Berg, W.J., Noël, B., Usher, M., 2014. Distinct patterns of seasonal Greenland glacier velocity. *Geophys. Res. Lett. 41*, 7209–7216. https://doi.org/10.1002/2014GL061836

Morlighem, M., Rignot, E., Binder, T., Blankenship, D., Drews, R., Eagles, G., Eisen, O., Ferraccioli, F., Forsberg, R., Fretwell, P., Goel, V., Greenbaum, J.S., Gudmundsson, H., Guo, J., Helm, V., Hofstede, C., Howat, I., Humbert, A., Jokat, W., Karlsson, N.B., Lee, W.S., Matsuoka, K., Millan, R., Mouginot, J., Paden, J., Pattyn, F., Roberts, J., Rosier, S., Ruppel, A., Seroussi, H., Smith, E.C., Steinhage, D., Sun, B., Broeke, M.R. van den, Ommen, T.D. van, Wessem, M. van, Young, D.A., 2020. Deep glacial troughs and stabilizing ridges unveiled beneath the margins of the Antarctic ice sheet. *Nat. Geosci. 13*, 132–137. https://doi.org/10.1038/s41561-019-0510-8

Mouginot, J., 2017. MEaSUREs Antarctic Boundaries for IPY 2007-2009 from Satellite Radar, Version 2. https://doi.org/10.5067/AXE4121732AD

Mouginot, J., Scheuchl, B., Rignot, E., 2012. Mapping of Ice Motion in Antarctica Using Synthetic-Aperture Radar Data. *Remote Sens. 4*, 2753–2767. https://doi.org/10.3390/rs4092753

Nagler, T., Rott, H., Hetzenecker, M., Wuite, J., Potin, P., 2015. The Sentinel-1 Mission: New Opportunities for Ice Sheet Observations. *Remote Sens. 7*, 9371–9389. https://doi.org/10.3390/rs70709371

Nagler, T., Wuite, J., Libert, L., Hetzenecker, M., Keuris, L., Rott, H., 2021. Continuous Monitoring of Ice Motion and Discharge of Antarctic and Greenland Ice Sheets and Outlet Glaciers by Sentinel-1 A amp; B, in: 2021 IEEE International Geoscience and Remote Sensing Symposium IGARSS. Presented at the 2021 IEEE International Geoscience and Remote Sensing Symposium IGARSS, pp. 1061–1064. https://doi.org/10.1109/IGARSS47720.2021.9553514

595   Naughten, K.A., Meissner, K.J., Galton-Fenzi, B.K., England, M.H., Timmermann, R., Hellmer, H.H., 2018. Future Projections of Antarctic Ice Shelf Melting Based on CMIP5 Scenarios. *J. Clim. 31*, 5243–5261. https://doi.org/10.1175/JCLI-D-17-0854.1

Paolo, F.S., Fricker, H.A., Padman, L., 2015. Volume loss from Antarctic ice shelves is accelerating. *Science 348*, 327–331. https://doi.org/10.1126/science.aaa0940

600   Paolo, F.S., Padman, L., Fricker, H.A., Adusumilli, S., Howard, S., Siegfried, M.R., 2018. Response of Pacific-sector Antarctic ice shelves to the El Niño/Southern Oscillation. *Nat. Geosci. 11*, 121–126. https://doi.org/10.1038/s41561-017-0033-0

Park, J.W., Gourmelen, N., Shepherd, A., Kim, S.W., Vaughan, D.G., Wingham, D.J., 2013. Sustained retreat of the Pine Island Glacier. *Geophys. Res. Lett. 40*, 2137–2142. https://doi.org/10.1002/grl.50379

605   Petty, A.A., Holland, P.R., Feltham, D.L., 2014. Sea ice and the ocean mixed layer over the Antarctic shelf seas. *The Cryosphere 8*, 761–783. https://doi.org/10.5194/tc-8-761-2014

Pritchard, H.D., Arthern, R.J., Vaughan, D.G., Edwards, L.A., 2009. Extensive dynamic thinning on the margins of the Greenland and Antarctic ice sheets. *Nature 461*, 971–975. https://doi.org/10.1038/nature08471

Pritchard, H.D., Ligtenberg, S.R.M., Fricker, H.A., Vaughan, D.G., Van Den Broeke, M.R., Padman, L., 2012. Antarctic ice-
610   sheet loss driven by basal melting of ice shelves. *Nature 484*, 502–505. https://doi.org/10.1038/nature10968

Rack, W., Rott, H., 2004. Pattern of retreat and disintegration of the Larsen B ice shelf, Antarctic Peninsula. *Ann. Glaciol. 39*, 505–510. https://doi.org/10.3189/172756404781814005

Rignot, E., 2016. MEaSUREs Antarctic Grounding Line from Differential Satellite Radar Interferometry, Version 2. https://doi.org/10.5067/IKBWW4RYHF1Q

615   Rignot, E., Casassa, G., Gogineni, P., Krabill, W., Rivera, A.U. and Thomas, R., 2004. Accelerated ice discharge from the Antarctic Peninsula following the collapse of Larsen B ice shelf. *Geophysical research letters*, 31(18). https://doi.org/10.1029/2004GL020697

Rignot, E., Jacobs, S., Mouginot, J., Scheuchl, B., 2013. Ice-Shelf Melting Around Antarctica. *Science 341*, 266–270. https://doi.org/10.1126/science.1235798

620   Rignot, E., Mouginot, J., Morlighem, M., Seroussi, H., Scheuchl, B., 2014. Widespread, rapid grounding line retreat of Pine Island, Thwaites, Smith, and Kohler glaciers, West Antarctica, from 1992 to 2011. *Geophys. Res. Lett. 41*, 3502–3509. https://doi.org/10.1002/2014GL060140

Rignot, E., Mouginot, J., Scheuchl, B., 2011a. Ice flow of the Antarctic Ice Sheet. *Science 333*, 1427–1430. https://doi.org/10.1126/science.1208336

625   Rignot, E., Mouginot, J., Scheuchl, B., 2011b. Antarctic grounding line mapping from differential satellite radar interferometry. *Geophys. Res. Lett. 38*. L10504, https://doi.org/10.1029/2011GL047109

Rignot, E., J. Mouginot, and B. Scheuchl. 2017. MEaSUREs InSAR-Based Antarctica Ice Velocity Map, Version 2. Boulder, Colorado USA. NASA National Snow and Ice Data Center Distributed Active Archive Center. https://doi.org/10.5067/D7GK8F5J8M8R. [Accessed January 2022].

630 Rignot, E., Mouginot, J., Scheuchl, B., Van Den Broeke, M., Van Wessem, M.J. and Morlighem, M., 2019. Four decades of Antarctic Ice Sheet mass balance from 1979–2017. *Proceedings of the National Academy of Sciences, 116*(4), 1095-1103. https://doi.org/10.1594/PANGAEA.896940).

Rosen, P.A., Hensley, S., Joughin, I.R., Li, F.K., Madsen, S.N., Rodriguez, E., Goldstein, R.M., 2000. Synthetic aperture radar interferometry. *Proc. IEEE 88*, 333–382. https://doi.org/10.1109/5.838084

635 Rott, H., Skvarca, P. and Nagler, T., 1996. Rapid collapse of northern Larsen ice shelf, Antarctica. *Science, 271*(5250), 788-792. https://doi.org/10.1126/science.271.5250.788

Rott, H., Wuite, J., De Rydt, J., Gudmundsson, G.H., Floricioiu, D. and Rack, W., 2020. Impact of marine processes on flow dynamics of northern Antarctic Peninsula outlet glaciers. *Nature communications, 11*(1), 1-3. https://doi.org/10.1038/s41467-020-16658-y

640 Scambos, T.A., Hulbe, C., Fahnestock, M. and Bohlander, J., 2000. The link between climate warming and break-up of ice shelves in the Antarctic Peninsula. *Journal of Glaciology*, 46(154), pp.516-530. https://doi.org/10.3189/172756500781833043

Scambos, T.A., Bohlander, J.A., Shuman, C.A. and Skvarca, P., 2004. Glacier acceleration and thinning after ice shelf collapse in the Larsen B embayment, Antarctica. *Geophysical Research Letters, 31*, L18402, 645 https://doi.org/10.1029/2004GL020670

Schannwell, C., Cornford, S., Pollard, D., Barrand, N.E., 2018. Dynamic response of Antarctic Peninsula Ice Sheet to potential collapse of Larsen C and George VI ice shelves. *The Cryosphere, 12*, 2307–2326. https://doi.org/10.5194/tc-12-2307-2018

Schoof, C., 2010. Ice-sheet acceleration driven by melt supply variability. *Nature*, 468(7325), pp.803-806. 650 https://doi.org/10.1038/nature09618

Selley, H.L., Hogg, A.E., Cornford, S., Dutrieux, P., Shepherd, A., Wuite, J., Floricioiu, D., Kusk, A., Nagler, T., Gilbert, L. and Slater, T., 2021. Widespread increase in dynamic imbalance in the Getz region of Antarctica from 1994 to 2018. *Nature communications, 12*(1), 1-10. https://doi.org/10.1038/s41467-021-21321-1

Selmes, N., Murray, T. and James, T.D., 2011. Fast draining lakes on the Greenland Ice Sheet. *Geophysical Research Letters*, 655 38(15). https://doi.org/10.1029/2011GL047872

Seroussi, H., Nowicki, S., Payne, A.J., Goelzer, H., Lipscomb, W.H., Abe-Ouchi, A., Agosta, C., Albrecht, T., Asay-Davis, X., Barthel, A., Calov, R., Cullather, R., Dumas, C., Galton-Fenzi, B.K., Gladstone, R., Golledge, N.R., Gregory, J.M., Greve, R., Hattermann, T., Hoffman, M.J., Humbert, A., Huybrechts, P., Jourdain, N.C., Kleiner, T., Larour, E., Leguy, G.R., Lowry, D.P., Little, C.M., Morlighem, M., Pattyn, F., Pelle, T., Price, S.F., Quiquet, A., Reese, R., 660 Schlegel, N.-J., Shepherd, A., Simon, E., Smith, R.S., Straneo, F., Sun, S., Trusel, L.D., Van Breedam, J., van de Wal,

R.S.W., Winkelmann, R., Zhao, C., Zhang, T., Zwinger, T., 2020. ISMIP6 Antarctica: a multi-model ensemble of the Antarctic ice sheet evolution over the 21st century. *The Cryosphere 14,* 3033–3070. https://doi.org/10.5194/tc-14-3033-2020

Steig, E.J., Ding, Q., Battisti, D.S., Jenkins, A., 2012. Tropical forcing of Circumpolar Deep Water Inflow and outlet glacier thinning in the Amundsen Sea Embayment, West Antarctica. *Ann. Glaciol. 53*, 19–28. https://doi.org/10.3189/2012AoG60A110

Stevens, L.A., Behn, M.D., McGuire, J.J., Das, S.B., Joughin, I., Herring, T., Shean, D.E. and King, M.A., 2015. Greenland supraglacial lake drainages triggered by hydrologically induced basal slip. *Nature*, 522(7554), pp.73-76. https://doi.org/10.1038/nature14480

Tedesco, M., Willis, I.C., Hoffman, M.J., Banwell, A.F., Alexander, P. and Arnold, N.S., 2013. Ice dynamic response to two modes of surface lake drainage on the Greenland ice sheet. *Environmental Research Letters*, 8(3), p.034007. https://doi.org/10.1088/1748-9326/8/3/034007

The IMBIE team, 2018. Mass balance of the Antarctic Ice Sheet from 1992 to 2017. *Nature, 558*(7709), 219-222. https://doi.org/10.1038/s41586-018-0179-y

Thoma, M., Jenkins, A., Holland, D., Jacobs, S., 2008. Modelling Circumpolar Deep Water intrusions on the Amundsen Sea continental shelf, Antarctica. *Geophys. Res. Lett. 35*. L18602, https://doi.org/10.1029/2008GL034939

Trusel, L.D., Frey, K.E., Das, S.B., Munneke, P.K., Broeke, M.R. van den, 2013. Satellite-based estimates of Antarctic surface meltwater fluxes. *Geophys. Res. Lett. 40*, 6148–6153. https://doi.org/10.1002/2013GL058138

Turner, J., Lu, H., White, I., King, J.C., Phillips, T., Hosking, J.S., Bracegirdle, T.J., Marshall, G.J., Mulvaney, R., Deb, P., 2016. Absence of 21st century warming on Antarctic Peninsula consistent with natural variability. *Nature 535*, 411–415. https://doi.org/10.1038/nature18645

Vaughan, D.G., Smith, A.M., Nath, P.C., Meur, E.L., 2003. Acoustic impedance and basal shear stress beneath four Antarctic ice streams. *Ann. Glaciol. 36*, 225–232. https://doi.org/10.3189/172756403781816437

Vieli, A., Nick, F.M., 2011. Understanding and Modelling Rapid Dynamic Changes of Tidewater Outlet Glaciers: Issues and Implications. *Surv. Geophys. 32*, 437–458. https://doi.org/10.1007/s10712-011-9132-4

Webber, B.G., Heywood, K.J., Stevens, D.P., Dutrieux, P., Abrahamsen, E.P., Jenkins, A., Jacobs, S.S., Ha, H.K., Lee, S.H. and Kim, T.W., 2017. Mechanisms driving variability in the ocean forcing of Pine Island Glacier. *Nature communications*, 8(1), pp.1-8. https://doi.org/10.1038/ncomms14507

Winter, K., Hill, E. A., Gudmundsson, G. H., and Woodward, J., 2020. Subglacial topography and ice flux along the English Coast of Palmer Land, Antarctic Peninsula, *Earth Syst. Sci. Data*, 12, 3453–3467, https://doi.org/10.5194/essd-12-3453-2020

Wuite, J., Rott, H., Hetzenecker, M., Floricioiu, D., De Rydt, J., Gudmundsson, G.H., Nagler, T., Kern, M., 2015. Evolution of surface velocities and ice discharge of Larsen B outlet glaciers from 1995 to 2013. *The Cryosphere 9*, 957–969. https://doi.org/10.5194/tc-9-957-2015

695 Zwally, H.J., Abdalati, W., Herring, T., Larson, K., Saba, J. and Steffen, K., 2002. Surface melt-induced acceleration of Greenland ice-sheet flow. *Science*, 297(5579), pp.218-222. https://doi.org/10.1126/science.1072708